POLITECNICO DI TORINO
Repository ISTITUZIONALE

# Revealing the competitive effect of N2 and H2O towards CO2 adsorption in N-rich ordered mesoporous carbons

*Original*
Revealing the competitive effect of N2 and H2O towards CO2 adsorption in N-rich ordered mesoporous carbons / Maruccia, E.; Piovano, A.; Lourenço, M. A. O.; Priamushko, T.; Cavallo, M.; Bocchini, S.; Bonino, F.; Pirri, F.; Kleitz, F.; Gerbaldi, C.. - In: MATERIALS TODAY SUSTAINABILITY. - ISSN 2589-2347. - STAMPA. - 21:(2023), p. 100270. [10.1016/j.mtsust.2022.100270]

*Availability:*
This version is available at: 11583/2973993 since: 2022-12-20T11:08:53Z

*Publisher:*
Elsevier

*Published*
DOI:10.1016/j.mtsust.2022.100270

*Terms of use:*

This article is made available under terms and conditions as specified in the corresponding bibliographic description in the repository

*Publisher copyright*

(Article begins on next page)

12 October 2024

Materials Today Sustainability 21 (2023) 100270

Contents lists available at ScienceDirect

Materials Today Sustainability

journal homepage: https://www.journals.elsevier.com/materials-today-sustainability

# Revealing the competitive effect of $N_2$ and $H_2O$ towards $CO_2$ adsorption in N-rich ordered mesoporous carbons

E. Maruccia [a, b, c, d, *], A. Piovano [b, c, e], M.A.O. Lourenço [a, g], T. Priamushko [d, h], M. Cavallo [c, e], S. Bocchini [a], F. Bonino [c, e], F.C. Pirri [a, f], F. Kleitz [d], C. Gerbaldi [b, c, **]

[a] Center for Sustainable Future Technologies (CSFT), Istituto Italiano di Tecnologia (IIT), Via Livorno, 60, 10144 Torino, Italy
[b] GAME Lab, Department of Applied Science and Technology, Politecnico di Torino, Corso Duca Degli Abruzzi, 24, 10129, Torino, Italy
[c] National Reference Center for Electrochemical Energy Storage (GISEL) - INSTM, Via G. Giusti 9, Firenze 50121, Italy
[d] Department of Inorganic Chemistry – Functional Materials, Faculty of Chemistry, University of Vienna, Währinger Strasse 42, 1090 Vienna, Austria
[e] Department of Chemistry, NIS and INSTM Centre, University of Torino, Via P. Giuria 7, 10125, Torino, Italy
[f] Department of Applied Science and Technology, Politecnico di Torino, Corso Duca Degli Abruzzi, 24, 10129, Torino, Italy

ARTICLE INFO

*Article history:*
Received 21 July 2022
Received in revised form
25 October 2022
Accepted 26 October 2022
Available online 12 November 2022

*Keywords:*
Ordered mesoporous carbon
N-rich carbon
Nanocasting
$CO_2$ capture
Gas separation
Renewable feedstock

ABSTRACT

The incorporation of heteroatoms improves $CO_2$ adsorption on carbon-based materials, but it can also provide some hydrophilic character to the bare-carbon frameworks, making the hypothesis of competitive $CO_2/H_2O$ adsorption not negligible. In this respect, the $CO_2$ capture is here evaluated through a deep characterization of the sorption properties of N-rich ordered mesoporous carbons under dry and moisture conditions, and in $CO_2/N_2$ gas mixtures. The nanocasting strategy is used to obtain N-rich CMK-3-type carbons in one pot by impregnating D-glucosamine hydrochloride, a carbon/nitrogen source, into an SBA-15 silica template followed by pyrolysis treatment at 600, 750, and 900 °C. The fine-tuning of the pyrolysis treatment aims to find the right proportion of micropores and N content, which are important features for selective $CO_2$ adsorption. The highest surface amount of N (11.3 at.%), in particular of the pyridinic type, enhances the $CO_2/N_2$ selectivity (1.03 mmol/g of adsorbed $CO_2$ from a 20% $CO_2$ in $N_2$), but also the undesired increment in the $H_2O$ uptake. $CO_2$ uptake under competitive $CO_2/H_2O$ conditions is better preserved with 8.3 at.% of surface nitrogen (1.55, 1.52, 0.61, and 0.89 mmol/g of $CO_2$ at a relative humidity of 0, 25, 50, and 75%, respectively). Interestingly, the N-CMK-3 materials retain their capture properties over repetitive adsorption-desorption cycles in pure $CO_2$. In this respect, a TGA-FTIR study is performed to monitor the reusability of the sorbents after $CO_2$ capture from moist flue gases to assess the effectiveness of the reactivation procedure towards the removal of the adsorbed species.
© 2022 The Author(s). Published by Elsevier Ltd. This is an open access article under the CC BY-NC-ND license (http://creativecommons.org/licenses/by-nc-nd/4.0/).

## 1. Introduction

Anthropogenic greenhouse gas (GHG) emissions are the main reason for the climate change phenomena that Earth is experiencing nowadays. GHG effect already caused an increase of 1.09 °C (0.95–1.20) of the global surface average temperature in the period 2011–2020 compared to pre-industrial times [1]. Unfortunately, this trend is expected to constantly grow, aggravated by the expansion of human needs consequent to the increase of the world population, unless strict measures are urgently adopted. Hence, new regulations have been recently introduced to guide the necessary climate actions, since the international agreement in Paris in 2015 to commit the 196 involved countries to keep the average increase in the global temperature well below 2 °C, preferentially below 1.5 °C, with respect to pre-industrial levels [3]. These targets have been renewed during COP26, which took place in Glasgow in 2021. The new targets include also the drastic reduction of emissions by 2030, aiming to reach net-zero emissions by the middle of the century.

Currently, the attention is meanly directed toward $CO_2$, which among the GHGs plays the main role in the alteration of the energy balance of the Earth-atmosphere system. Nowadays, Carbon Capture and Storage (CCS) technologies represent a robust strategy for

* Corresponding author.
** Corresponding author.
*E-mail addresses:* elisa.maruccia@polito.it (E. Maruccia), claudio.gerbaldi@polito.it (C. Gerbaldi).
[g] Present Address. CICECO - Aveiro Institute of Materials, Department of Chemistry, University of Aveiro, Campus Universitário de Santiago, Aveiro, 3810-193, Portugal.
[h] Present Address. Helmholtz Institute Erlangen-Nürnberg for Renewable Energy (IEK-11) - Forschungszentrum Jülich GmbH, Electrocatalysis, Team Electrochemical Energy Conversion, Cauerstraβe 1, Erlangen, 91058, Germany.

https://doi.org/10.1016/j.mtsust.2022.100270
2589-2347/© 2022 The Author(s). Published by Elsevier Ltd. This is an open access article under the CC BY-NC-ND license (http://creativecommons.org/licenses/by-nc-nd/4.0/).

tackling $CO_2$ sequestration, and post-combustion capture has the advantage of being easily retrofitted in existing plants. At present, solvent-based $CO_2$ absorption by aqueous amine solutions is the most mature technology [4,5]. However, amine scrubbing processes are affected by some drawbacks. Particularly, amine degradation generates products that are corrosive to the equipment and toxic to human beings and the environment [6]. Moreover, the energy penalty due to amine-based sorbents regeneration hampers the extensive implementation of this technology [7,8]. Carbon capture strategies based on the adsorption process using porous materials are attractive due to reducing the energy consumption on sorbents regeneration and also overcoming the issues related to corrosion and toxicity [7,9]. Zeolite [10], metal-organic frameworks (MOFs) [11], amino-functionalized porous silicas [12], and carbon-based materials [13] are among the most exploited sorbents for $CO_2$ capture. An interesting analysis regarding the technical-economic aspects of post-combustion $CO_2$ capture was carried out by Subraveti et al., who investigated the main attributes of an ideal adsorbent and compared it with monoethanolamine-based absorbents, reveling that an optimized adsorption process has the potential to be more convenient than absorption, not only from an energetic but also from an economic point of view [14].

The typical composition of post-combustion flue gases is approximatively 73–77% $N_2$, 15–16% $CO_2$, 5–7% $H_2O$ and 3–4% $O_2$ in coal-fired power plants [15] and 67–72% $N_2$, 8–10% $CO_2$, 18–20% $H_2O$ and 2–3% $O_2$ in natural gas-fired power plants [16]. The separation of $CO_2$ from a mixture containing $N_2$ and $H_2O$ vapor requires the development of adsorbents with characteristics such as high selectivity for $CO_2$ capture and robustness in humid environments [17]. Generally, the effect of the presence of water vapor in flue gas mixtures has to be carefully taken into consideration, since most sorbents based on silica [18], zeolites [9,19,20], and MOFs [21], undergo a reduction in their $CO_2$ capture performances, due to structural instability under humid conditions and/or competitive adsorption caused by their strong affinity for $H_2O$. In this case, a pre-condensation of water was recommended by Ben-Mansour and coworkers [22], who investigated the $CO_2$ adsorption by a MOF sorbent from dry and humid $CO_2/N_2$ mixtures through both numerical simulations analysis and lab experiments. On the contrary, $CO_2$ adsorption by amine-functionalized carbon sorbents benefits from the presence of a proper amount of water, as demonstrated by Lourenço et al. [23] and Wu et al. [24]. For these kinds of sorbents, it is believed that water plays a crucial role in the formation of carbamate ions by the reaction of $CO_2$ molecules with the amine groups of the sorbents [25]. Moreover, the formed carbamate ion or the amino group itself can subsequently react with $CO_2$ and $H_2O$ molecules to form bicarbonate ions [26].

Many recent works addressed the problem of the preservation of good $CO_2$ adsorption performances from wet flue gases by water-sensitive sorbents like MOFs [22,27–32] and zeolites [33,34]. On the contrary, the problem of water presence in post-combustion flue gases is usually considered less crucial for carbon materials, due to their intrinsic hydrophobic nature and remarkable tolerance toward moisture [35]. However, the absence of polar groups in hydrophobic carbons limits the efficiency of selective $CO_2$ removal in real flue gas mixtures [9]. Hence, O and N are often introduced into the bare-carbon frameworks to enhance the affinity for $CO_2$, increasing at the same time the surface polarity and providing some hydrophilic character to the carbon surface [36], interacting with water via hydrogen bonding [37,38].

In this work, the influence of water contamination on the selective $CO_2$ capture from simulated post-combustion flue gases by nitrogen-doped carbonaceous adsorbents was investigated. Sorbents with a high affinity toward $CO_2$ were prepared through a direct route that avoids post-synthesis functionalization methods. Hence, a nanocasting synthesis procedure was here employed as a handy and affordable method for the preparation of mesoporous carbons with well-defined porous characteristics. Precisely, SBA-15 ordered mesoporous silica was used as a hard template and D-glucosamine (an abundant component in biomass residues) was chosen as a sustainable, concurrent carbon/nitrogen (C/N) source, to produce CMK-3-type N-containing ordered mesoporous carbons (named, NOMCs). The adsorption performances of the adsorbents were studied, focusing firstly on the evaluation of single component $CO_2$ and $H_2O$ adsorption, and subsequently, on the evaluation of the selective $CO_2$ capture from dry ($CO_2/N_2 = 20/80$ v/v) and wet ($CO_2/H_2O$, a relative humidity (RH) ranging from 0 to 75%) simulated flue gas mixtures, respectively. Finally, the reusability of the sorbents was also considered to provide a thorough evaluation of the potential applicability of the synthesized materials in industrial applications.

## 2. Experimental

### 2.1. Synthesis

The SBA-15 silica hard template was synthesized following the procedure described by Guillet-Nicolas et al. [39]. Precisely, 8 g of poly(ethylene glycol)-block-poly(propylene glycol)-block-poly(ethylene glycol) ($EO_{20}PO_{70}EO_{20}$, P123, Sigma-Aldrich MW~5800) was dissolved at 35 °C in 150 mL of 0.3 M hydrochloric acid (HCl, VWR, 37%) aqueous solution. When P123 was completely dissolved, 13 g of tetraethyl orthosilicate (TEOS, Sigma-Aldrich 98%) was added to the mixture and let stir at the same temperature. After 24 h, the mixture was hydrothermally treated at 100 °C for 48 h under static conditions. The hot solution was filtered and dried in an oven at 140 °C. P123 was removed by solvent extraction in ethanol/HCl solution ($C_2H_6O$, EtOH, Brenntag, 96%) and then by calcination at 550 °C. The nitrogen-containing N-CMK-3-type carbons were prepared following the procedure described in our recent work [40]. Briefly, the SBA-15 silica template (degassed overnight at 150 °C under vacuum) was impregnated with an aqueous solution of D-glucosamine hydrochloride ($C_6H_{13}NO_5 \cdot HCl$, Alfa Aesar, >98%) and sulfuric acid ($H_2SO_4$, VWR, 95%) using a two steps procedure. Precisely, for 1 g of SBA-15, 1.58 g of D-glucosamine hydrochloride, 0.097 mL of $H_2SO_4$, and 6 g of deionized water were impregnated in the first step, while in the second step, 0.96 g of D-glucosamine hydrochloride, 0.06 mL of $H_2SO_4$ and 3.66 g of $H_2O$ were used. The slurry was stirred for 1 h at room temperature until a homogeneous gel-like consistency was obtained and then thermally treated in a calcination furnace at 100 °C for 6 h, 140 °C for 2 h, and 160 °C for 6 h (heating rate 150 °C/min) during the first impregnation, and at 100 °C for 6 h, and 140 °C for 2 h during the second impregnation step. The resulting powders were moved into a quartz reactor with a capillary cap design [41,42] and pyrolyzed at 600, 750, or 900 °C (heating rate 3 °C/min) for 4 h in a calcination furnace in the air under atmospheric pressure. The two intermediate steps at 200 °C for 6 h and at 655 °C for 4 h (except for the sample pyrolyzed at 600 °C) were introduced before reaching the final pyrolysis temperature ($T_p$). The silica removal step was made by dissolving the silica in a 2 M sodium hydroxide (NaOH, 98%, flakes) water/ethanol solution ($H_2O$:ethanol = 1:1, v/v) at room temperature and overnight. This step was repeated more than two times. The samples underwent several repetitive washing steps in water and ethanol and were finally dried overnight at 70 °C. The obtained materials had been denominated N-CMK-3_X, where X is the pyrolysis temperature (i.e., 600, 750, or 900 °C).

### 2.2. Characterization

The experimental methodology adopted to characterize the synthesized samples is described in detail in the Supporting Information (SI) and summarized in Table 1.

**Table 1**
Summary of the experimental methodology adopted to characterize the synthesized samples.

| Technique | Equipment | Characterization details |
|---|---|---|
| LAXRD[a] | EMPYREAN diffractometer + PIXcel3D detector (Malvern PANalytical, United Kingdom) | Transmission mode; Cu $K_{\alpha 1+2}$ radiation ($\lambda$ = 0.154 nm); Operating voltage: 45.0 kV; Tube current: 40.0 mA; $2\theta$ step size: 0.013°; data time per step: 50 s. |
| TEM[b]/STEM[c] | Tecnai $G^2$ F20 S-twin microscope (FEI Technologies Inc., USA) + BF[d]/HAADF[e] detectors | Acceleration voltage: 200 kV; Sample dispersed in high purity ethanol and drop-casted onto lacey-carbon Cu TEM grids. |
| $N_2$ sorption @−196 °C: SSA[f] and mesoporosity | IQ2 instrument + AsiQwin 5.2 software (Anton Paar QuantaTech Inc., USA) | Degassing in vacuum: 12 h, 150 (silica) or 300 °C (carbons); Models: BET[g], NLDFT[h] (silica, cylindrical pores) or QSDFT[i] (carbon, cylindrical pores). |
| $CO_2$ sorption: 1) microporosity 2) $K_H$[j] 3) $\Delta H$ [k] $_{ads,CO2}$ | IQ2 instrument + AsiQwin 5.2 software (Anton Paar QuantaTech Inc., USA) | 1) T = 0 °C, degassing in vacuum: 12 h, 300 °C; Models: NLDFT (carbon); 2) T = 0 °C, degassing in vacuum: 12 h, 300 °C; Virial isotherm model 3) T = −10, 0, 10 °C; degassing in vacuum: 12 h, 300 °C; Clausius-Clapeyron equation. |
| XPS[l] | PHI 5000 VersaProbe (Physical Electronics, Minnesota, USA) + OriginPro 2020 software (OriginLab Corporation, USA) | Al Kα radiation (1486.6 eV); Pass energy: 187.75 eV (survey spectrum), and 23.5 eV (HR[m] spectra); X-ray beam diameter: 100 μm. HR[m] spectra fit with Gaussian functions and background subtraction with a spline. |
| TGA[n]-$CO_2/N_2$ selectivity | TG 209 F1 Libra | T = 35 °C, p = 1 bar; Activation in $N_2$: 300 °C, 30 min (10 °C/min); Gas mixture: $CO_2/N_2$ = 20/80 v/v. |
| Adsorption-desorption 4) $CO_2$ 5) $H_2O$ ($\Delta H$ads[o] $_{,H2O}$) 6) $CO_2/H_2O$ 7) Cyclic $CO_2$ | Dynamic Vapor Sorption (DVS) instrument (Surface Measurement System, United Kingdom) | Activation in vacuum: 300 °C, 30 min; Equilibrium criterion: dm/dt = 0.002% $min^{-1}$ 4) T = 30 °C, p = 90%* $p^p_{CO2sat,T}$; 5) T = 30–60 °C, p = 90%*$p^q_{H2Osat,T}$; 6) T = 30 °C, p = 0 −90%*$p^q_{H2Osat,T}$, RH[r]: 0 −75%. 7) T = 30 °C, p = 20%* $p^p_{CO2sat,T}$. Regeneration in a vacuum: 150 °C |
| $N_2$ sorption @−196 °C (reusability assessment) | 3Flex equipment (Micromeritics Instrument Corporation, USA) | Activation in vacuum: 300 °C; Model: NLDFT[h] (cylindrical pores) |
| TGA-FTIR[s] spectroscopy | TG 209 F1 Libra + Bruker Tensor II equipped with IR gas cell + FT-IR[s] Coupling Systems (Netzsch, Germany) | T = 25–800 °C, 20 °C/min, $N_2$ flow; Activation in $N_2$: 300 °C, 30 min (10 °C/min); IR spectra of the evolved gases sampled at 3 °C intervals |

(*continued on next page*)

**Table 1** (*continued*)

[a] LAXRD: low-angle X-ray diffraction.
[b] TEM: transmission electron microscopy.
[c] STEM: scanning transmission electron microscopy.
[d] BF: bright-field.
[e] HAADF: high-angle annular dark-field.
[f] SSA: specific surface area.
[g] BET: Brunauer-Emmett-Teller.
[h] NLDFT: non-local density functional theory.
[i] QSDFT: quenched solid density functional theory.
[j] $K_H$: Henry's law constant.
[k] $\Delta H$ads$_{,CO2}$: isosteric enthalpy of $CO_2$ adsorption.
[l] XPS: X-ray photoelectron spectroscopy.
[m] HR: high resolution.
[n] TGA: thermogravimetric analysis.
[o] $\Delta H$ads$_{,H2O}$: isosteric enthalpy of $H_2O$ adsorption.
[p] $p_{CO2sat,T}$: $CO_2$ saturation pressure at T.
[q] $p_{H2Osat,T}$: $H_2O$ saturation pressure at T.
[r] RH: relative humidity.
[s] FTIR: Fourier transform infrared.

## 3. Results and discussion

### 3.1. Textural properties

The textural properties of the N-CMK-3_X materials were determined by analyzing the samples by LAXRD, TEM, and $N_2$ physisorption. Fig. S3b presents the LAXRD patterns of the N-CMK-3_X carbon replicas, that seem to possess a similar arrangement of the pores (*p6mm* hexagonal symmetry) [43] to the parent SBA-15 silica template (Fig. S3a). The parent silica shows the typical three well-resolved peaks indexed as (100), (110), and (200) planes, while the N-CMK-3_X replicas only display the (100) reflection. Noteworthy, the increase of the $T_p$ above 750 °C improved the pore organization. The XRD unit cell size $a_{100}$ was calculated from the (100) reflection using the expression $a_{100} = \frac{2}{\sqrt{3}} \cdot d_{100}$ [44], where the interplanar spacing $d_{100}$ was calculated using Bragg's law. The high-temperature treatment causes shrinkage of the mesostructure in a higher magnitude as long as $T_p$ increases [45,46], as observed by the reduction of the interplanar *d*-spacing and, consequently, of the unit cell size (Table 2). The periodic alignment of the channel-like pores, according to the typical arrangement of N-CMK-3-type materials, is also evident from the TEM/STEM images shown in Fig. 1 and Fig S4, which were obtained using different objectives apertures to optimize the image contrast.

The $N_2$ adsorption-desorption isotherms (at −196 °C) are type IVa isotherms, which are typically observed for (ordered) mesoporous materials (Figs. S5a–b and Fig. 2a), with some character of type I, for all the samples [47]. At a relative pressure ($p/p_0$) within the range of 0.4–0.9, capillary condensation inside mesopores occurred, while a further increase of the adsorbed volume at $p/p_0 >$ 0.9 can be ascribed to adsorption in larger-sized interparticle voids [48]. The QSDFT model was selected to calculate the specific surface area and the mesopore size distribution of the N-CMK-3_X samples, as it fits well the experimental data (Fig. S6, SM).

Although the Rouquerol criteria partially helped in overcoming the complexity of determining the linear range of relative pressure where BET is applicable, BET surface area calculated with isotherms obtained on microporous materials does not represent the real probe accessible surface, but only an apparent surface area [49]. On the contrary, in our case, the surface area and porosity parameters calculated with the QSDFT method are

**Table 2**
Physicochemical properties of the N-CMK-3 samples.

| | $a_{100}$[a] nm | $S_{BET}$ m$^2$/g | $S_{DFT}$[b] m$^2$/g | $V_p$[b] cm$^3$/g | $D_p$[b] nm | $V_{ump}$[c] cm$^3$/g | $V_{mp}$[c] cm$^3$/g | $D_{mp}$[c] nm |
|---|---|---|---|---|---|---|---|---|
| SBA-15 | 11.9 | 719 | 598 | 1.0 | 8.8 | – | – | – |
| N-CMK-3_600 | 10.2 | 605 | 672 | 0.4 | 4.1 | 0.12 | 0.16 | 0.5; 0.8 |
| N-CMK-3_750 | 9.2 | 656 | 921 | 0.6 | 4.4 | 0.12 | 0.19 | 0.5; 0.8 |
| N-CMK-3_900 | 9.2 | 667 | 818 | 0.5 | 4.5 | 0.14 | 0.23 | 0.5; 0.8 |

[a] Unit cell size ($a_{100}$) calculated using the expression $a_{100} = \frac{2}{\sqrt{3}} \cdot d_{100}$

[b] Specific surface area ($S_{DFT}$), pore volume ($V_p$), and pore width ($D_p$) in the mesoporous range, calculated by NLDFT and QSDFT methods for silica and carbons, respectively, applied to $N_2$ isotherms at −196 °C.

[c] Ultramicropore volume ($V_{ump}$), micropore volume ($V_{mp}$), and pore width ($D_{mp}$) of N-CMK-3 samples in the microporous range, calculated by the NLDFT method, applied to $CO_2$ isotherms at 0 °C.

considered more reliable, by taking into account not only the geometry of the pores but also the solid-fluid interaction and surface roughness [49–52]. The mesopore size distribution (PSD) is narrow and centered approximately at 4.5 nm (see inset in Fig. 2a) for the samples N-CMK-3_750 and N-CMK-3_900. Conversely, the sample N-CMK-3_600 shows lower specific surface area and pore volume and a less narrow pore size distribution in comparison to the other samples of the series, in line with the lower quality XRD pattern and TEM image. According to the findings of Zhang et al. [53], the slight collapse of the ordered mesoporous architecture could occur during the drying step in the synthesis procedure of the N-CMK-3_600 sample, which contains a higher surface concentration of heteroatoms (see Paragraph 3.2), therefore presents a higher hydrophilic character in comparison to the other samples of the N-CMK-3 series. The micro- and ultramicroporosity were specifically analyzed via $CO_2$ adsorption isotherms at 0 °C (Fig. 2b). $CO_2$ was chosen as the preferred gas probe to benefit from the smaller kinetics diameter and the higher absolute temperature and pressure of analysis than $N_2$ sorption at cryogenic temperature. Hence, both the gas probe diffusion and accessibility in the very narrow pores ($D_p$ < 0.4 nm) increased, as already demonstrated in the literature [47,48,54]. From the observation of Fig. 2b, it is possible to see the presence of microporosity in N-CMK-3 samples, consisting of two populations of micro- and ultramicropores, with the maximum of the populations found at 0.8 and 0.5 nm, respectively. The physicochemical parameters derived from $N_2$ and $CO_2$ sorption analysis are summarized in Table 2.

### 3.2. Physicochemical properties

The CMK-3-type NOMCs samples are mainly constituted by C (78.9, 79.1, and 83.4 at.%), O (8.4, 8.9, and 9.4 at.%), and N (11.3, 8.3, and 4.4 at. %) elements, for N-CMK-3_600, N-CMK-3_750 and N-CMK-3_900, respectively, as derived from the XPS survey spectra in Fig. S7. The increment of $T_p$ leads to the increase of the surface C relative amount as a consequence of the loss of heteroatoms [55]. Therefore, the highest surface atomic concentration of N was found in the sample N-CMK-3_600. Residual amounts of Na (<2 at.%), S (<0.5 at.%) and Si (<0.7 at.%) were observed in all samples. Both Na and S are derived from the synthesis procedures, while the latter is related to the remaining silica hard template, which is anyhow negligible, thus confirming the successful removal of the template. The adventitious contaminations of S and Na might both positively contribute to $CO_2$ capture, since S-doping is another strategy proposed in the literature to enhance the efficiency of the process [56–59] and a recent theoretical study envisaged the same effect on carbon models with a high loading of alkali metals (around 10 at.%) [60]. Since in our case the amount of S and Na inclusions is very low and randomly distributed in the series of samples, we can safely neglect their contribution with respect to the more abundant and properly modulated incorporation of N-species. High-resolution (HR) acquisitions were performed in C1s, N1s, and O1s regions to investigate the chemical bonding state of the most relevant elements. From C1s core level peaks, we were able to observe three different carbon species (see Figs. S8a, S9a, and S10a in SM) assigned to C–C sp$^2$ (284.3–284.8 eV), CO/C–N (285.9–286.5 eV), and C=O/C=N (286.5–287.6 eV) [61,62]. Oxygen signals (see Figs. S8c, S9c, and S10c in SM) were fitted by using three components assigned to C=O (~ 531 eV), C–O (~ 533 eV), and COOH (~ 534 eV) [62], while the deconvolution of the N1s peak of NOMCs revealed three components assigned to pyridinic (C=N–C, N-6, 397.7–398.9 eV), pyrrolic (C–NH–C, N-5, 399.9–400.7 eV), and graphitic (C–NH–C, N-Q, 401.0–401.8 eV) nitrogen-based structures (Figures S8b, S9b and S10b in SM) [61]. The relative percentages of each component were calculated from the fitted

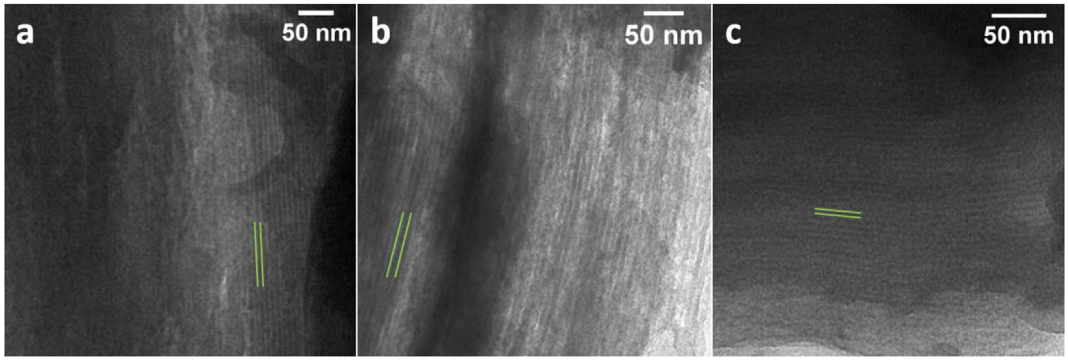


**Fig. 1.** TEM micrographs of (a) N-CMK-3_600, (b) N-CMK-3_750, (c) N-CMK-3_900 samples.

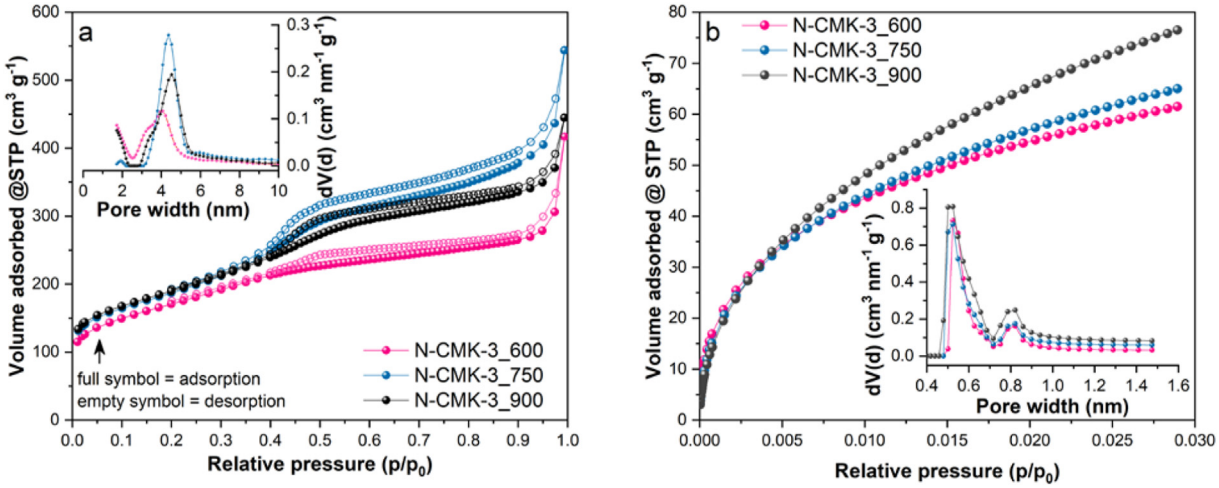


**Fig. 2.** (a) $N_2$ adsorption-desorption isotherms at −196 °C and in the inset the QSDFT pore size distribution in the mesoporous range of NOMC samples, i.e., N-CMK-3_600, N-CMK-3_750, and N-CMK-3_900 (pink, cyan, and black profiles, respectively), and (b) $CO_2$ adsorption-desorption isotherms at 0 °C and in the inset the NLDFT pore size distribution in the microporous range of NOMC samples, i.e., N-CMK-3_600, N-CMK-3_750, and N-CMK-3_900 (pink, cyan, and black profiles, respectively).

peak areas quantified by the deconvolution of the HR-XPS signals in the C1s, N1s, and O1s regions. The summary of the quantities derived from the XPS analysis is reported in Table 3.

It is possible to observe that the graphitization degree of the N-CMK-3_X samples increases with the rise of the temperature, observed by the increase of the C−C $sp^2$ and C=X relative contents. The evolution of nitrogen-containing moieties is related to their different thermal stability. The fraction of N-6 and N-5 decreases with the increase of $T_p$ from 600 to 900 °C because they are both transformed into N-Q in the pyrolysis temperature range of 600−800 °C [63]. Accordingly, N-Q is detected in a higher concentration in the sample pyrolyzed at 900 °C. The O-functionalities are less sensitive to the thermal treatment; indeed, their relative percentage was found to be approximately unmodified in all the N-CMK-3 samples under study.

### 3.3. Pure $CO_2$ adsorption measurements

The isosteric enthalpy of $CO_2$ adsorption ($-\Delta H_{ads,CO2}$) as a function of the surface coverage (i.e., $CO_2$ adsorbed amount in mmol/g), is shown in Fig. 3b.$-\Delta H_{ads,CO2}$ was calculated for the N-CMK-3-type samples from the adsorption branches of the $CO_2$ isotherms obtained at −10, 0, and 10 °C in Fig. S11 using the Clausius-Clapeyron approach. The main contribution to $-\Delta H_{ads,CO2}$ at low coverage is given by the occupation of the adsorption sites associated with a stronger affinity for $CO_2$ [64]. At higher surface loadings, $-\Delta H_{ads,CO2}$ decreases as a function of the coverage and stabilizes roughly to the heat of liquefaction of $CO_2$, i.e., approximately 17 kJ/mol in the considered temperature range, because at this point the system is approaching the pore filling regime, where adsorbate-adsorbate interactions govern the mechanism of adsorption [65]. The values of $-\Delta H_{ads,CO2}$ calculated for the N-CMK-3 samples synthesized in this work lay in the range of 30−38 kJ/mol, which is attributable to a physisorption mechanism (from 25 to 50 kJ/mol) [66]. The values of $-\Delta H_{ads,CO2}$ stay within an optimal energetic range (30−50 kJ/mol) for achieving concurrently efficient adsorption and easy regeneration [7,67]. Henry's constant ($K_H$) and the virial coefficients $C_1$ e $C_2$ were also calculated from the $CO_2$ isotherms at 0 °C (Fig. S12) and listed in Table S1 in SM. $K_H$ values follow the inverse trend of the pyrolysis temperature as a consequence of the loss of heteroatoms during the high-temperature heat treatment, as was already observed in our previous work [40].

N-CMK-3_600 material better performed in the pure $CO_2$ adsorption (precisely 7.3 wt%, i.e., 1.66 mmol/g of adsorbed $CO_2$) at 30 °C (Fig. 3a). This result is associated with the highest value of $K_H$ (Table S1), which in turn derives from the high amount of N species, especially of the pyridinic type, present in the sample. Conversely, the N-CMK-3_900 sample provided the lowest $CO_2$ adsorption at 30 °C, equal to 3.7 wt%, i.e., 0.83 mmol/g. The pure $CO_2$ uptake in the N-CMK-3_900 sample is mainly ascribed to the microporosity, due to the lower contribution derived from the surface N content. Indeed, the positive effect of micro- and ultramicroporosity on the uptake undergoes a more pronounced reduction than surface chemistry by increasing the test temperature [68]. Conversely, this difference is less pronounced in the samples pyrolyzed at lower temperatures, both for the already mentioned N-CMK-3_600 and also the N-CMK-3_750, which showed intermediate performances (6.8 wt%, i.e., 1.55 mmol/g of adsorbed $CO_2$). This behavior further confirms that N species play a beneficial role in the $CO_2$ uptake, especially at temperatures close to ambient temperature [69].

### 3.4. Reusability assessment by multiple $CO_2$ adsorption-desorption cycles

Ten cycles of adsorption-desorption were performed on N-CMK-3 samples to assess the reusability of the sorbents (Fig. 4). The samples under study showed good reproducibility upon repetitive use under pure $CO_2$ adsorption measurements at 30 °C and at 20 kPa (0.2 bar). The regeneration of the sorbents was carried out by heating up to 150 °C between consecutive cycles (TSA process). The highest efficiency loss (up to ca. 10 and 16% for N-CMK-3_600 and N-CMK-3_900 samples, respectively) occurred between the first and the second cycle. For both samples, a certain amount of $CO_2$ cannot be desorbed during the regeneration step at 150 °C, likely because the adsorbate is strongly bonded to the high-energy N-sites in the case of N-CMK-3_600, or trapped in the micropores as for the N-CMK-3_900. After the second cycle, all the N-CMK-3 studied samples proved to be stable and the adsorbed amount was almost unvaried. This evidence demonstrated that the sorbents can be reused in multiple adsorption/desorption cycles from dry flue

**Table 3**
Summary of the XPS analysis on the survey and high-resolution spectra of the C1s, N1s, and O1s region for the N-CMK-3 samples.

| Sample name | Peak | Amount[a] at.% | Binding energy eV | Assignment | Fitted peak area counts $s^{-1}$ | Fitted peak area[b] (%) |
|---|---|---|---|---|---|---|
| N-CMK-3_600 | C1s | 78.9 | 284.7 | C−C | 2835.0 ± 9.3 | 69.83 |
| | | | 285.8 | C−O/C−N | 939.2 ± 10.1 | 23.13 |
| | | | 287.1 | C=O/C=N | 285.6 ± 10.7 | 7.04 |
| | N1s | 11.3 | 398.4 | C=N−C | 442.9 ± 5.6 | 46.12 |
| | | | 400.4 | C−NH−C | 454.4 ± 8.2 | 47.30 |
| | | | 401.3 | C−NC−C | 63.2 ± 8.3 | 6.58 |
| | O1s | 8.4 | 530.9 | C=O | 698.3 ± 33.3 | 48.70 |
| | | | 532.5 | C−O | 560.4 ± 22.0 | 39.08 |
| | | | 533.5 | COOH | 175.2 ± 13.1 | 12.22 |
| N-CMK-3_750 | C1s | 79.1 | 284.8 | C−C | 4813.3 ± 14.0 | 71.67 |
| | | | 285.9 | C−O/C−N | 1156.9 ± 16.6 | 17.23 |
| | | | 286.6 | C=O/C=N | 745.7 ± 17.9 | 11.10 |
| | N1s | 8.3 | 398.4 | C=N−C | 477.3 ± 8.7 | 39.00 |
| | | | 400.3 | C−NH−C | 335.8 ± 19.1 | 27.44 |
| | | | 401.1 | C−NC−C | 410.8 ± 14.6 | 33.56 |
| | O1s | 8.9 | 530.9 | C=O | 794.9 ± 8.8 | 48.30 |
| | | | 532.5 | C−O | 586.4 ± 11.6 | 35.64 |
| | | | 533.5 | COOH | 264.3 ± 12.7 | 16.06 |
| N-CMK-3_900 | C1s | 83.4 | 284.8 | C−C | 4860.8 ± 11.0 | 70.68 |
| | | | 286.2 | C−O/C−N | 1202.8 ± 11.9 | 17.49 |
| | | | 287.6 | C=O/C=N | 813.1 ± 16.0 | 11.83 |
| | N1s | 4.4 | 398.5 | C=N−C | 248.5 ± 6.5 | 35.94 |
| | | | 399.9 | C−NH−C | 115.2 ± 8.6 | 16.66 |
| | | | 401.1 | C−NC−C | 327.7 ± 28.6 | 47.40 |
| | O1s | 9.4 | 530.9 | C=O | 616.2 ± 7.9 | 46.72 |
| | | | 532.5 | C−O | 527.1 ± 12.4 | 39.98 |
| | | | 533.5 | COOH | 175.4 ± 11.4 | 13.30 |

[a] Derived from the XPS survey scan.
[b] The percent fitted peak area is here considered as an indication of the relative amount of each species in the sample.

gases without losing their performances and, in addition, be satisfactorily regenerated under mild conditions.

### 3.5. $CO_2/N_2$ adsorption measurements

TGA measurements were performed at 35 °C and 1 bar exposing the samples to a mixture that simulates a typical exhaust gas (20 vol% $CO_2$ and 80 vol% of $N_2$) [70], to evaluate the competitive adsorption of these two gases (Fig. 5). N-CMK-3_600 sample achieved an improved selectivity in $CO_2/N_2$ mixture, measured as a 4.52 wt% weight increase (1.03 mmol/g). Indeed, the N-CMK-3_600 sample benefits from the higher surface N content and, particularly, the superior concentration of pyridinic-N inclusions, which allowed for enhanced $CO_2$ uptake in comparison to the N-CMK-3_750 and N-CMK-3_900 samples, which achieved 4.36 wt% (0.99 mmol/g) and 3.69 wt% (0.84 mmol/g), respectively. Similarly to what was observed for the pure $CO_2$ adsorption measurement, the increase of the pyrolysis temperature promotes a decrease in the selectivity towards $CO_2$ in the $N_2/CO_2$ separation process, which can be associated with the lower quantity of N-6 species in the materials pyrolyzed at higher temperature (*cf.* XPS quantification in Table 3). Indeed, pyridinic-N inclusions are considered to provide the strongest contribution to $CO_2$ adsorption among the other types of N-containing functional groups, thanks to the strong basicity, derived from the lone pair electrons of the N atom which establishes a Lewis acid-base interaction with the electron-deficient carbon atom of the $CO_2$ molecule [40,71,72]. Moreover, the work of Lin et al. [73] also demonstrated the highest difference between

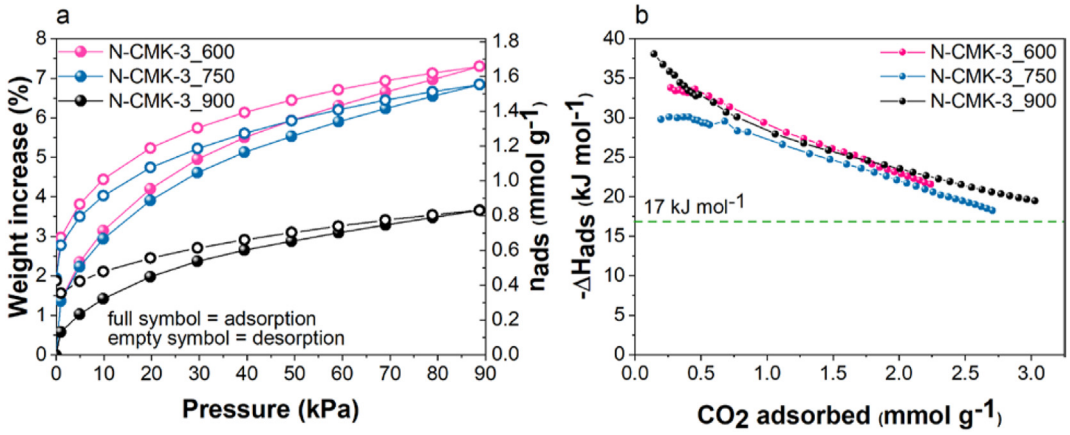


**Fig. 3.** Pure $CO_2$ adsorption-desorption isotherms measured at 30 °C up to 90 kPa with a gravimetric sorption analyzer (see Fig. S2a in SM), (b) isosteric enthalpy of $CO_2$ adsorption calculated in the temperature range between −10 and 10 °C vs. the $CO_2$ adsorbed for the N-CMK-3 samples under study. The green dashed line describes the heat of liquefaction of $CO_2$ in the temperature range considered.

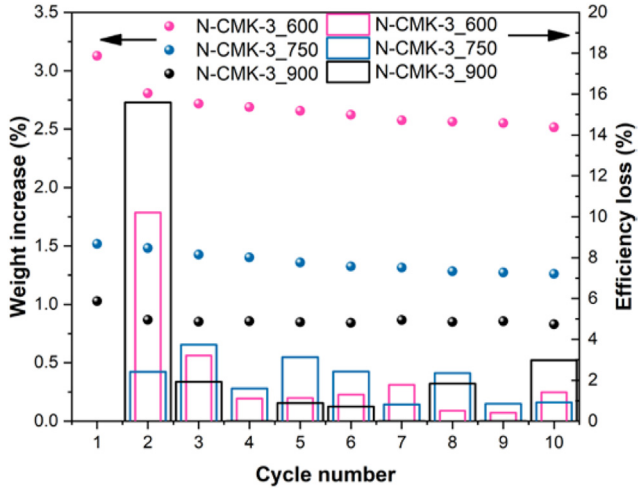


**Fig. 4.** Reusability tests of the studied N-CMK-3 samples under repetitive adsorption (30 °C) - desorption (150 °C) cycles at 0.2 bar (see Fig. S2d in SM). The efficiency loss is calculated with respect to the previous cycle.

$CO_2$ and $N_2$ adsorption energies for the pyridinic group compared to several analyzed N-functionalities, including pyrrolic and quaternary N, thus resulting in improved $CO_2/N_2$ selectivity [73]. The regenerability of the sorbents was also considered by the quantification of the percentage of released $CO_2$ in PSA conditions. As for the PSA approach, the promotion of the desorption of $CO_2$ by simply applying a flow of $N_2$ is more convenient from an energetic point of view than the TSA condition effectively applied in Paragraph 3.4. It is interesting to observe in Fig. 5a that almost the overall amount of the adsorbed $CO_2$ is released in PSA conditions (−2.90, −2.68, and −2.55 for N-CMK-3_600, N-CMK-3_750 and N-CMK-3_900, respectively). Then, heating was applied to remove the strongly bounded $CO_2$. At T < 150 °C, most of the adsorbed $CO_2$ is released. Also under these conditions, the adsorption capacity and selectivity results are consistent with the trend of the calculated $K_H$ values (see Fig. 5b and Table S1 in SM).

### 3.6. $H_2O$ adsorption measurements

Single component $H_2O$ adsorption isotherms were performed at 30 °C to compare this result with $CO_2$ adsorption (Fig. 6a). It is worth taking into consideration that owing to the relatively unstable $H_2O$ adsorption observed by the as-synthesized samples, which revealed their poor hydrophilic character, the isotherms reported in Fig. 6a are obtained after previous $H_2O$ adsorption measurements at 30 °C. As a result, the carbon-based adsorbents display an increased affinity to water after a previous adsorption of water, as shown in Fig. S13, in agreement with the mechanism of adsorption governed by cluster formation hypothesized by Horikawa et al. [74]. In detail, the $H_2O$ vapor adsorption-desorption curves in Fig. 6 and S14 present a sort of type IV isotherm (IUPAC denomination) [47], characterized by Type I character at very low partial pressure [36], indicative of an onset of water adsorption at very low pressure. A change in the concavity of the adsorption/desorption branches describes a two-stage-adsorption mechanism, which involves firstly the filling of micropores in the low relative pressure regime and subsequently of mesopores at higher pressure. In our case, the growing trend of total adsorbed water while increasing the analysis temperature is ascribable to the higher water vapor saturation pressure ($p_{H2Osat,T}$), which allows for conducting the analysis at increased absolute pressure values. Indeed, in the relatively low-pressure regime, the amount of adsorbed $H_2O$ is higher for the isotherms obtained at lower analysis temperatures. From the reported data, it is possible to observe that $H_2O$ adsorption is higher in the N-CMK-3_600 sample than for N-CMK-3_750 and N-CMK-3_900 ones. This evidence is consistent with the predictions since the more abundant incorporation of heteroatoms (namely O and N) in the carbon framework obtained at the lowest $T_p$ provides a stronger hydrophilic character. Indeed, N and O species are considered to promote water adsorption, especially in the low and intermediate pressure region [74,75], and according to the study of Kumar et al. [38], water vapor adsorption is more influenced by the local density of N species than their type. Despite an increased affinity for $H_2O$ given by heteroatoms incorporation inside the pristine carbon surface, the N-CMK-3-type samples studied in this work exhibited still a poor hydrophilic character when compared to other highly hydrophilic N-doped carbons, which achieved 4–5 orders of magnitude higher $H_2O$ uptake in the low relative pressure range [36]. This conclusion is particularly encouraging from the perspective of the original application of the N-CMK-3 sorbents studied in this work as selective $CO_2$ sorbents from moisture flue gases. Analogous observations are also derived from the quantification of the isosteric enthalpy of water adsorption ($-\Delta H_{ads,H2O}$). In the considered loading range, the $\Delta H_{ads,H2O}$ values of all the N-CMK-3 samples (see Fig. 6b) are below the

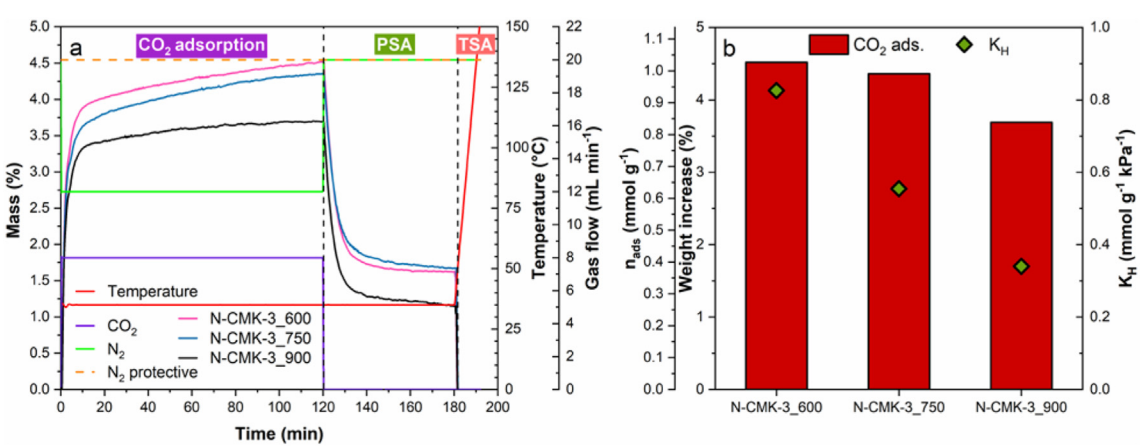


**Fig. 5.** (a) Adsorption and desorption steps and (b) weight increase due to the $CO_2$ adsorption in a gas mixture of 20 vol % $CO_2$ and 80 vol % of $N_2$ at 35 °C for $CO_2/N_2$ adsorption measurements by the N-CMK-3 samples under study. Details on setup for $CO_2/N_2$ selectivity tests by TGA in Fig. S1 in SM.

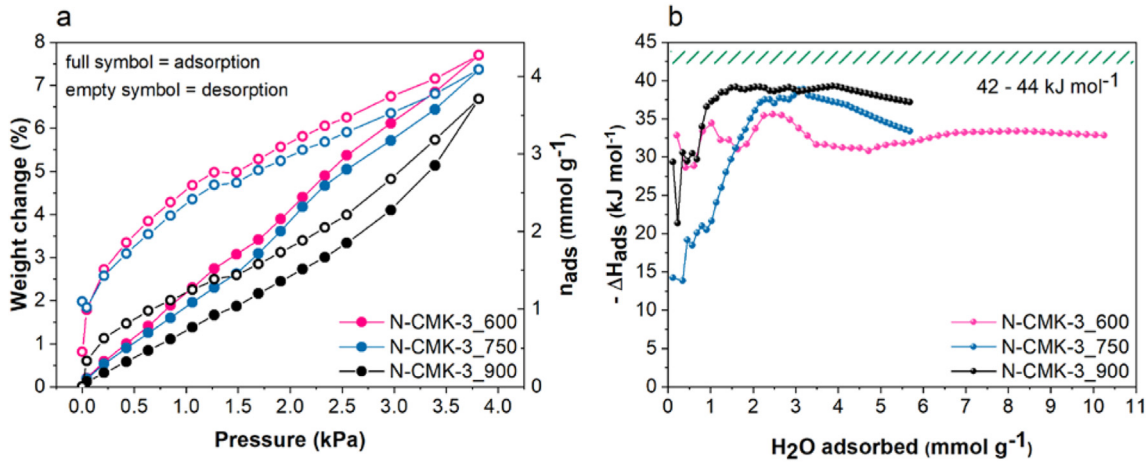


**Fig. 6.** Pure $H_2O$ vapor sorption isotherms were measured at 30 °C with a gravimetric sorption analyzer (see Fig. S2b in SM). The weight change is plotted against the absolute pressure (kPa): N-CMK-3_600 (pink dots), N-CMK-3_750 (cyan dots), and N-CMK-3_900 (black dots) samples. b) $\Delta H_{ads,H2O}$ plotted against the $H_2O$ adsorbed amount was calculated in the 40–60 °C temperature range for N-CMK-3_600 (pink dots), N-CMK-3_750 (cyan dots), and N-CMK-3_900 (black dots) samples. The patterned green area describes the range of values for the water heat of condensation in the considered temperature range.

enthalpy of condensation of water, which lies approximately in the range 42–44 kJ/mol in the analyzed temperature range (30–60 °C) [76]. This indication confirms the hydrophobic nature of the NOMC samples studied in this work. However, despite the average behavior, the samples locally present some specific sites, such as micropores or O- or N- sites, where $-\Delta H_{ads,H2O}$ approaches the enthalpy of condensation of water. Precisely, the adsorbate-adsorbent interactions govern water adsorption at low coverage [77].

Hence, the initial modest values of $-\Delta H_{ads,H2O}$ for the N-CMK-3_750 sample likely derive from the lower N content, which causes a weaker affinity for the $H_2O$, with respect to the N-CMK-3_600 sample. In the case of the N-CMK-3_900 sample, the high content of micropores likely compensates for the low concentration of N-species. As the adsorption progresses, the energy involved in the water cluster formation becomes dominant and mostly influences $\Delta H_{ads,H2O}$ values.

### 3.7. $CO_2$ adsorption under humid conditions

Three consecutive $H_2O/CO_2$ adsorption-desorption cycles (the method used is schematically described in Fig. S2c) were performed at 30 °C on the two most promising samples (N-CMK-3_600 and N-CMK-3_750) to study the ability of the samples to capture $CO_2$ under humid condition. Fig. 7 shows the weight change of the samples resulting from the exposition to different mixtures of $H_2O$ and $CO_2$. During the 1st cycle (Fig. 7a and b), RH was kept constant at 25% (i.e., $p_{H2O} = 1.06$ kPa), while $CO_2$ partial pressure ($p_{CO2}$) was varied from 0 to 65% (i.e., from 0 to 2.76 kPa), in the assumption that $H_2O$ adsorption remains constant at the same absolute $H_2O$ pressure. An increment of $p_{CO2}$ at constant RH corresponds to an increase in the weight of the samples which is attributable to $CO_2$ adsorption. It is worth noticing that a certain amount of the adsorbed species did not desorb during the 1st cycle, thus occupying part of the available pore volume and, in turn, hindering the utilization of the maximum capacity of the sorbents during the subsequent cycles. The same adsorption behavior is observed during the 2nd cycle (Fig. 7c and d) when RH was kept constant at 50% and $p_{CO2}$ gradually increases from 0 to 40%.

However, it is promising to observe that the samples are still able to capture $CO_2$ even if water is previously adsorbed in the porosity of the samples and this increment of the sample weight is directly proportional to $p_{CO2}$. During the 3rd cycle (Fig. 7e and f), RH gradually increased and stabilized at 75%. Subsequently, 15% of $p_{CO2}$ was added. The introduction of $CO_2$ caused a remarkable increment of the weight correspondent to 2.9 and 3.9 wt% for N-CMK-3_600 and N-CMK-3_750 samples, respectively. Generally, the sample N-CMK-3_750 adsorbs a lower amount of $H_2O$, as observed also in single-component isotherms (see Fig. 6a and Fig. S14), and a higher amount of $CO_2$ in comparison to the sample N-CMK-3_600 under humid conditions.

Table 4 reports the amounts of $CO_2$ adsorbed under different conditions of humidity. The maximum amount of adsorbed $CO_2$ at RH = 25% is comparable to the one under pure $CO_2$ (reported in Fig. 3a), which means that a moderate presence of moisture does not affect the ability of the adsorbents to capture $CO_2$, especially for the N-CMK-3_750 sample. However, by rising the RH up to 75%, the amount of $CO_2$ adsorbed was significantly reduced. Nonetheless, this behavior is not linear. For instance, the quantity of the $CO_2$ adsorbed decreases after the increase of RH from 25% to 50%, but on the contrary, the adsorbed $CO_2$ amount increases from RH 50–75%. Similar behavior has already been reported in the literature [24–26], demonstrating that the effect of $H_2O$ on $CO_2$ adsorption is a balance between the competition towards the occupation of the adsorption sites and the promotion of side reactions at the N-species that consume $CO_2$ (e.g., bicarbonate formation). Considering the two examined samples, the lowest affinity for $H_2O$ shown by the N-CMK-3_750 sample, allowed higher retention of satisfying $CO_2$ capture capabilities in presence of water. This result makes it the most suitable sorbent among the studied ones for $CO_2$ capture under moisture conditions.

### 3.8. Assessment of sorbents reusability after $H_2O$ adsorption

The adsorption in pure $CO_2$ at 30 °C was repeated after the tests under humid gas mixtures (see Fig. S15), observing a considerable reduction in the $CO_2$ uptake after the exposition to water (−45% for N-CMK-3_600 and −65% for N-CMK-3_750). This might be related

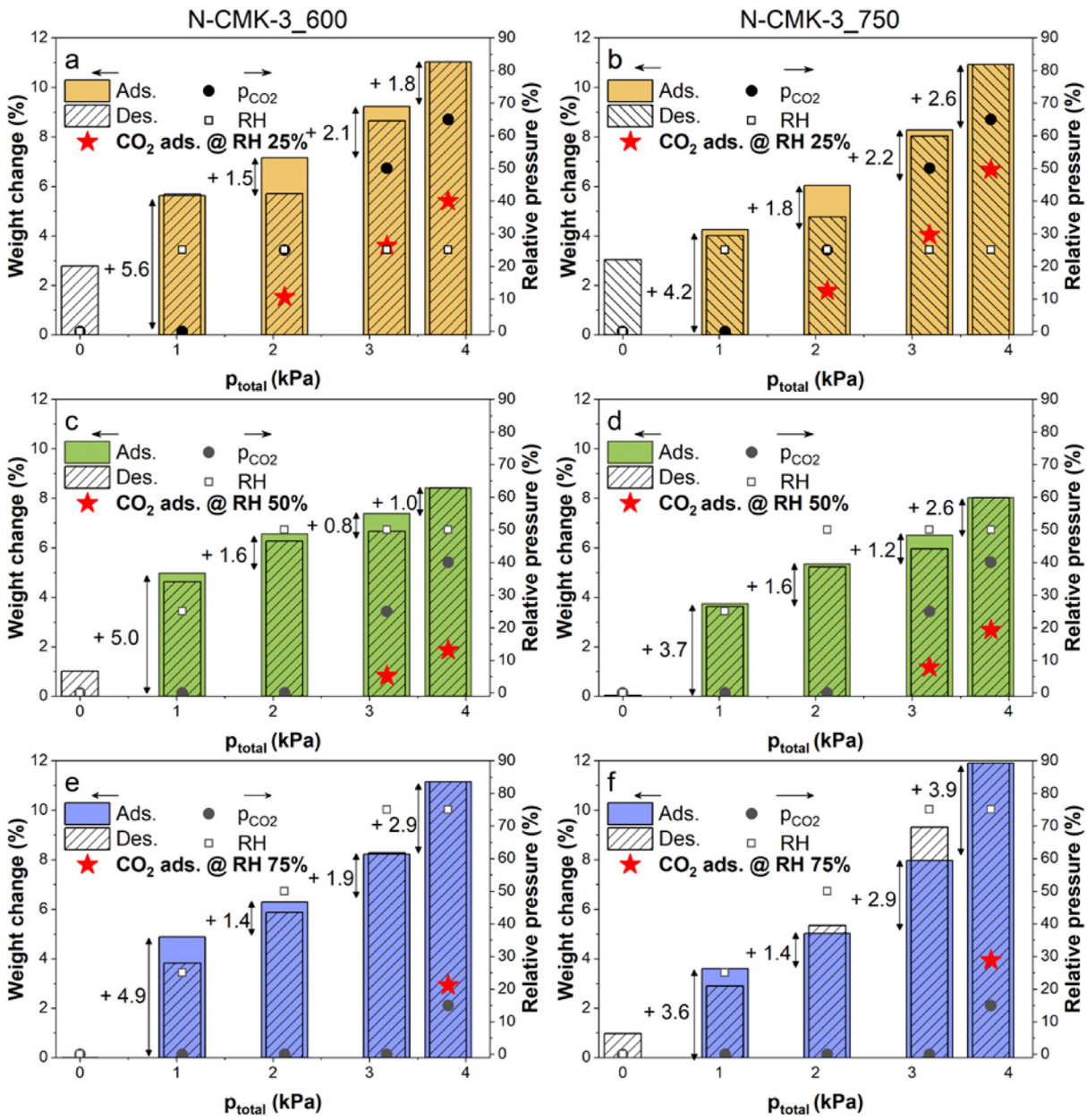


**Fig. 7.** Weight increase *vs* total pressure derived from cyclic $H_2O/CO_2$ adsorption-desorption tests performed at 30 °C at a different relative pressure of $H_2O$ and $CO_2$ according to the scheme in Fig. S2c. The data refer to the sample N-CMK-3_600 (a, c and e are for the 1st, 2nd, and 3rd adsorption/desorption cycle, respectively) and to the sample N-CMK-3_750 (b, d, and f are for 1st, 2nd, and 3rd adsorption/desorption cycle). For the 2nd and 3rd cycles, the residual adsorbed species from the previous cycles are counted in the initial weight. The arrows indicate the weight increase between two consecutive adsorption cycles and the star symbol indicates the weight increase due to $CO_2$ adsorption with respect to the weight increase achieved under pure $H_2O$ at the target RH.

either to the incomplete desorption of the adsorbates from the previous tests, even upon reactivation at 300 °C under vacuum, or to a structural collapse during the reactivation, promoted by the same trapped gases. Indeed, some irreversibility between adsorption and desorption was observed during the $CO_2/H_2O$ adsorption tests in Fig. 7, presumably not desorbed $H_2O$, since this species is more difficult to remove, owing to the higher isosteric enthalpy of water adsorption in respect to $CO_2$ [78]. As a matter of fact, at the end of the desorption branch of the 1st cycle, the final weight of the sample was around 3 wt% of the initial weight (see Fig. 7a and b). Further analysis of the textural features before and after the exposition to $H_2O$ on the N-CMK-3_600 sample was performed by $N_2$ adsorption-

**Table 4**
Maximum $CO_2$ adsorption at 30 °C under different humidity percentage for the N-CMK-3-type samples under study.

| Sample name | $CO_{2,ads}$ @ RH 0% mmol/g | $CO_{2,ads}$ @ RH 25% mmol/g | $CO_{2,ads}$ @ RH 50% mmol/g | $CO_{2,ads}$ @ RH 75% mmol/g |
|---|---|---|---|---|
| N-CMK-3_600 | 1.66 | 1.23 | 0.42 | 0.66 |
| N-CMK-3_750 | 1.55 | 1.52 | 0.61 | 0.89 |

desorption isotherms at −196 °C, to verify the more convincing hypothesis of unsuccessful regeneration as the main cause of the decrease of $CO_2$ uptake, even after the usual activation process at 300 °C preceding each measurement. This sample was chosen among the others of the N-CMK-3 series for its more marked hydrophilic character, derived from the higher content of N-species. The samples were activated at 300 °C in a vacuum for 1 h before the analysis, in line with the procedure used for the measurements under $CO_2/H_2O$ atmosphere. A further attempt was considered by extending the activation treatment up to 12 h to evaluate the potential beneficial effect of a longer treatment in improving the evacuation of the adsorbed species. The isotherms obtained in Fig. 8a of the fresh sample and the same sample treated in $H_2O$ and subsequently activated for 1 h or 12 h are the same original combination of type I plus IV, confirming the retention of the characteristic CMK-3 mesostructure. Similarly, the pore size distributions in the inset in Fig. 8b are all roughly comparable, except for the population of the smallest micropores (Ø < 1 nm, reasonably the most effective in $CO_2$ capture) that are completely disappeared, together with a specific family of quite small mesopores (Ø ≈ 2–2.5 nm). The fact that some pores populations remain totally unaffected while others completely disappeared unequivocally supports the hypothesis of pore occlusion by non-desorbed $H_2O$ molecules, rather than structure collapse during water adsorption tests and/or reactivation treatment.

As a consequence of pore occlusion, the sample treated in $H_2O$ shows a sizable reduction of the BET surface area, total pore volume, and micropore volume, even after the activation procedure, with a stronger deterioration, as predictable, in the case of the shortest regeneration treatment of 1 h. Precisely, a reduction of 60.6% of $S_{BET}$, 47.1% of $V_p$, and 89.6% of $V_{mp}$ was recorded in the case of the activation at 300 °C for 1 h. The longer treatment carried out at 12 h only slightly helped in restoring the initial textural features. The dramatic decrease of the micropore volume is the most remarkable information deduced from this analysis since this characteristic is important for $CO_2$ adsorption. Therefore, it is reasonable that the considerable reduction of the number of these preferential sites of adsorption is the cause of the inability to restore the initial uptake capability by the considered sample. To further investigate this phenomenon, a thermogravimetric analysis coupled with Fourier transform infrared spectroscopy (TGA-FTIR) on the N-CMK-3_600 sample was performed after $H_2O$ adsorption and compared with the fresh sample (see Fig. 9a and b). The TGA profile of the fresh sample (Fig. 9a) shows a first degradation peak at 70 °C, corresponding to a weight loss of about 8 wt%, then a constant limited loss of 6 wt% for temperatures varying from 100 to 600 °C and a final step of weight loss equal to ca. 10 wt% from 600 to 800 °C. The evolved gases are composed mainly of $H_2O$, $CO_2$, CO, $NH_3$, and HCN; their relative intensities change during the test, as shown in Fig. 9c. During the first step (Figs. S16a–b), the fresh sample mainly released $H_2O$ that was adsorbed from the atmosphere; in the second step (Fig. S16c), the main component of the evolved gas mixture is $CO_2$, while from temperatures higher than 600 °C, the weight loss slowly increases as expected from carbonaceous materials prepared at 600 °C. Indeed, in this phase (see Fig. S16d), the fresh carbon sample slowly evolves producing HCN and $NH_3$, thus reducing the quantity of nitrogen incorporated in the carbon framework, as expected based on the XPS analysis, and producing CO and $CO_2$ from material graphitization. The TGA-FTIR analysis on the sample tested in $H_2O$ adsorption, here labeled as "treated", shows several differences in comparison to the fresh sample. First, the thermodegradation curve exhibits a new step with a maximum at around 235 °C and a weight loss of ca. 20 wt% (Fig. S16e). In this range of temperatures, the IR spectra (see Figs. S16f–g) clearly show the presence of $CH_2$ moieties and carbonyl groups typical of ketones, carboxylic acids, etc. [79]. In addition, it is worth noticing that, differently from the fresh sample, at temperatures higher than 300 °C, the IR spectra of the treated sample show the release of $H_2O$ (see Fig. S16h), with a continuous increment of the intensity of the signal as long as the temperature increases (Fig. 8d).

In conclusion, the volumetric and thermogravimetric analyses considerably helped in extrapolating useful information regarding the optimal regeneration conditions for the studied sorbents after their exposition to moist environments. In detail, the usual activation process carried out at 300 °C was revealed to be not completely successful in evacuating the previously adsorbed species during $H_2O$ or $H_2O/CO_2$ adsorption tests. The attempt of keeping the same temperature (i.e., 300 °C) while prolonging the activation time was not fully successful to restore the initial properties of the sorbents so that to justify a longer time for the regeneration procedure, which is a collateral step of the capture process. On the contrary, the increase of the activation temperature, as suggested by the thermogravimetric analysis, could be more effective in totally restoring the initial adsorption capacity, but the feasibility of the process is still questionable in terms of energy consumption for a real application.

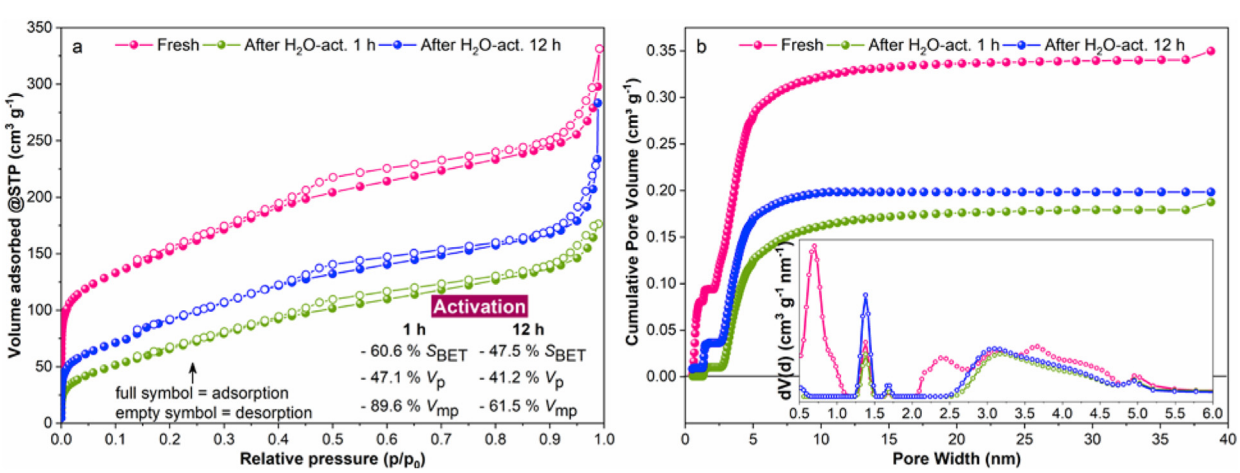


**Fig. 8.** Investigation of the change in the porosity properties of the N-CMK-3_600 sample before and after $H_2O$ adsorption: a) $N_2$ adsorption-desorption isotherms at −196 °C and, b) DFT cumulative pore volume and pore size distribution (inset) in the micro- and mesoporous range. The activation treatment was carried out at 300 °C in a vacuum for 1 h, in the case of the fresh sample and at 300 °C in a vacuum for 1 h or 12 h in the case of the same sample previously treated in $H_2O$.

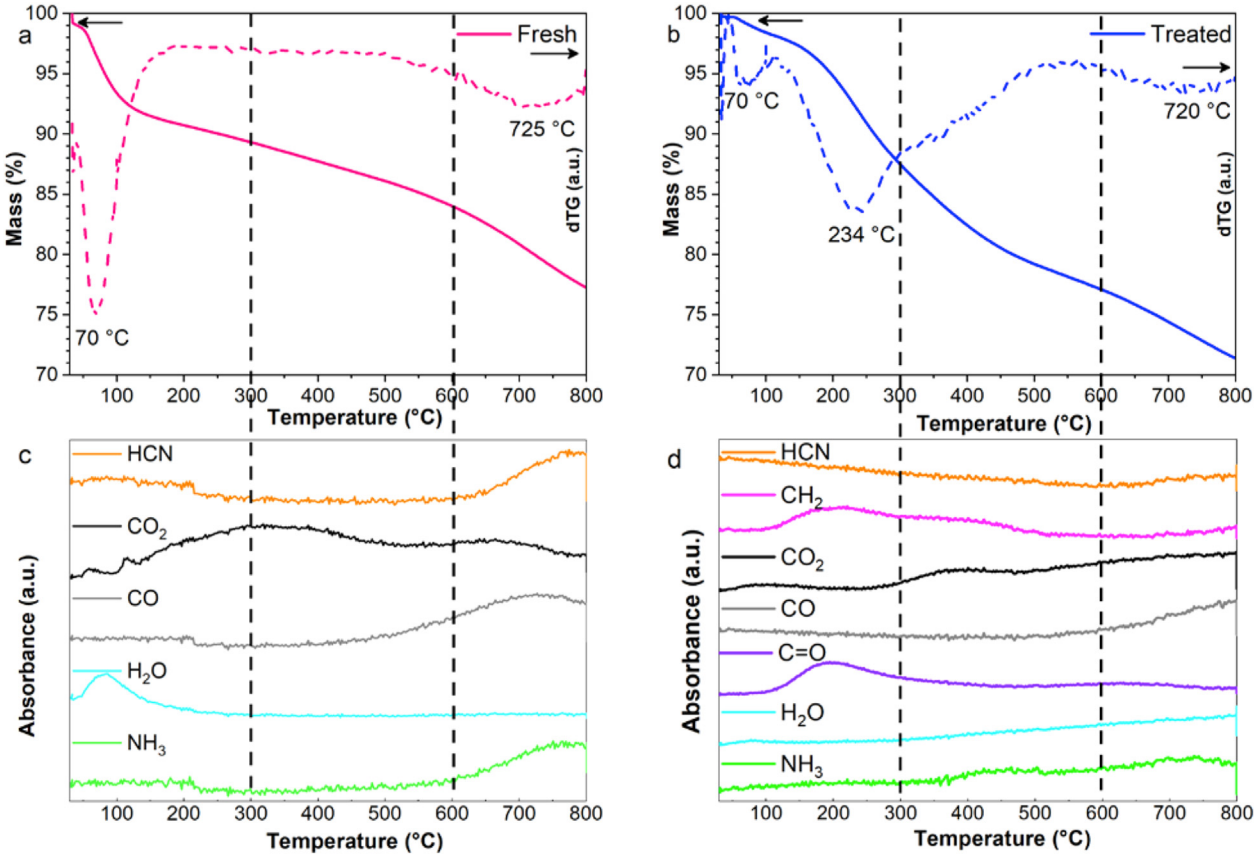


**Fig. 9.** TGA-FTIR analysis: a,b) mass change vs. temperature (wt.% vs. °C) and differential weight (dTG) vs. temperature (d%wt. d/C vs. °C) profiles of fresh N-CMK-3_600 sample and the same sample after $H_2O$ adsorption; c) intensity vs. temperature of the peaks relative to $NH_3$ at 965 $cm^{-1}$, $H_2O$ at 1505 $cm^{-1}$, CO at 2179 $cm^{-1}$, $CO_2$ at 2349 $cm^{-1}$, HCN at 3735 $cm^{-1}$ for fresh N-CMK-3_600 sample, and d) intensity vs. temperature of the peaks relative to $NH_3$ at 965 $cm^{-1}$, $H_2O$ at 1505 $cm^{-1}$ CO at 2179 $cm^{-1}$, $CO_2$ at 2349 $cm^{-1}$, HCN at 3735 $cm^{-1}$, paraffin by $-CH_2$ at 2925 $cm^{-1}$, oxidized paraffin by $-C{=}O$ at 1715 $cm^{-1}$ for the same sample after $H_2O$ adsorption [80–82].

## 4. Conclusions

This work investigated the $CO_2$ capture ability and selectivity over $N_2$ and $H_2O$ gases in simulated post-combustion flue gases by N-containing carbonaceous adsorbents. Three different N-containing ordered mesoporous carbons of the CMK-3-type were successfully synthesized through the nanocasting method of D-glucosamine on SBA-15 silica template. The pyrolysis temperature was adjusted to tune both the porosity features and the surface chemistry (e.g., N content) in a single step. It was observed that a higher N content improved both the $CO_2$ adsorption at a temperature close to room temperature and atmospheric pressure and the selectivity toward $CO_2$ in $CO_2/N_2$ gas mixtures. In this work, D-glucosamine was chosen as the nitrogen-rich carbon source, being sustainable and renewable, as extractable from chitin, the second most abundant natural polymer present in several biomass residues (e.g., insects, arachnids, or crustaceans) [83]. Furthermore, nanocasting from broadly available SBA-15 silica template worked as a standardized procedure for tuning both the porosity features and the surface chemistry in a single step, thus bypassing post-synthesis modification aimed at increasing micropore content and heteroatoms doping.

Specifically, a maximum $CO_2$ adsorption capacity of 1.66 mmol/g for pure $CO_2$, and 1.03 mmol/g for 20% $CO_2$ in $N_2$ was obtained for the sample with the highest N content (N-CMK-3_600, with 11.3 at.% of N). However, N species enhanced also the affinity for $H_2O$, so that the N-CMK-3_600 sample experienced a higher reduction in $CO_2/H_2O$ selectivity in comparison to the sample N-CMK-3_750, which contains a lower amount of nitrogen (8.3 at.%). Generally, despite an unavoidable reduction in the $CO_2$ uptake in humid gas mixtures, due to the competitive adsorption between $CO_2$ and $H_2O$, the studied samples still retained good $CO_2$ capture capability. As mentioned above, the N-CMK-3_750 sample better preserved the selectivity for $CO_2$ uptake in moist gas compositions with a $CO_2$ uptake of 1.52, 0.61, and 0.89 mmol/g at RH 25, 50, and 75%, respectively. However, the repetition of the $CO_2$ adsorption tests after $H_2O$ adsorption revealed a considerable reduction in the uptake, owing to the incomplete desorption of water mainly from very narrow micropores (Ø < 1 nm), thus making these binding sites unavailable for the subsequent capture of $CO_2$. Conversely, the retention of the $CO_2$ capture properties under repetitive sorption-desorption cycles was assessed by reusability tests in pure $CO_2$ flow, revealing almost unvaried performances even after 10 cycles. Only a slightly appreciable efficiency loss was registered between the first and the second cycle, but it is ascribed to irreversible sorption of $CO_2$ molecules, which stayed bound at the most energetic sites after the regeneration step at 150 °C. The hypothesis of the degradation of the samples was excluded because, after the second cycle, the $CO_2$ adsorption remained reproducible upon multiple cycles.

In summary, the obtained sorbents displayed good characteristics in terms of adsorption capacity, cyclability in pure $CO_2$, and selectivity in $CO_2/N_2$ and $CO_2/H_2O$ binary mixtures, in comparison with other materials reported in the literature (as in Table S2) [23,24,30,84–86]. Furthermore, this study satisfies the original aim to explore the competition between $H_2O$ and $CO_2$ from simulated

post-combustion flue gas mixtures onto N-rich carbons, to identify their potentiality and limits from a real application perspective. Therefore, in a future perspective, the identification of the ideal reactivation conditions for fully restoring the specific $CO_2$ adsorption sites from accidentally adsorbed $H_2O$ might be the decisive solution, to assure complete reusability of the sorbents applied for $CO_2$ capture from moist flue gases.

## Author contributions

The manuscript was written with the contributions of all authors. All authors have given approval to the final version of the manuscript.

## Funding sources

The RECODE project received funding from the EU's H2020 (R&I) programme under GA 768583. E.M., T.P., and F.K. acknowledge the funding support of the University of Vienna (Austria).

## Declaration of competing interest

The authors declare the following financial interests/personal relationships which may be considered as potential competing interests: Claudio Gerbaldi reports financial support was provided by European Commission.

## Data availability

Data will be made available on request.

## Acknowledgment

The RECODE project received funding from the EU's H2020 (R&I) programme under GA 768583. E.M., T.P., and F.K. acknowledge the funding support of the University of Vienna (Austria). The authors are thankful to Dr. Salvatore Guastella for XPS measurement in the core facility (Department of Applied Science and Technology, Politecnico di Torino), Dr. Marco Fontana for TEM images (Center for Sustainable Future Technologies (CSFT), Istituto Italiano di Tecnologia (IIT)) as well as to Dr. Giuseppe Ferraro Center for Sustainable Future Technologies (CSFT), Istituto Italiano di Tecnologia (IIT)) and Dr. Rémy Guillet-Nicolas (Department of Inorganic Chemistry – Functional Materials, University of Vienna) for technical support.

## Appendix A. Supplementary data

Supplementary data to this article can be found online at https://doi.org/10.1016/j.mtsust.2022.100270.

## References

[1] IPCC, V. Masson-Delmotte, P. Zhai, A. Pirani, S.L. Connors, C. Péan, S. Berger, N. Caud, Y. Chen, Climate Change 2021: the Physical Science Basis. Contribution of Working Group I to the Sixth Assessment Report of the Intergovernmental Panel on Climate Change, Cambridge Univ. Press, 2021, p. 3949. https://www.ipcc.ch/report/ar6/wg1/downloads/report/IPCC_AR6_WGI_Full_Report.pdf.

[3] J. Delbeke, A. Runge-Metzger, Y. Slingenberg, J. Werksman, The paris agreement, in: Towards a Climate Europe: Curbing the Trend, 2019, pp. 24–45, https://doi.org/10.4324/9789276082569-2.

[4] N. Harun, T. Nittaya, P.L. Douglas, E. Croiset, L.A. Ricardez-Sandoval, Dynamic simulation of MEA absorption process for $CO_2$ capture from power plants, Int. J. Greenh. Gas Control 10 (2012) 295–309, https://doi.org/10.1016/j.ijggc.2012.06.017.

[5] C.H. Yu, C.H. Huang, C.S. Tan, A review of $CO_2$ capture by absorption and adsorption, Aerosol Air Qual. Res. 12 (2012) 745–769, https://doi.org/10.4209/aaqr.2012.05.0132.

[6] M. Khraisheh, S. Mukherjee, A. Kumar, F. Al Momani, G. Walker, M.J. Zaworotko, An overview on trace $CO_2$ removal by advanced physisorbent materials, J. Environ. Manage. 255 (2020), 109874, https://doi.org/10.1016/j.jenvman.2019.109874.

[7] M. Oschatz, M. Antonietti, A search for selectivity to enable $CO_2$ capture with porous adsorbents, Energy Environ. Sci. 11 (2018) 57–70, https://doi.org/10.1039/c7ee02110k.

[8] F. Hussin, M.K. Aroua, Recent trends in the development of adsorption technologies for carbon dioxide capture: a brief literature and patent reviews (2014–2018), J. Clean. Prod. 253 (2020) 119707, https://doi.org/10.1016/j.jclepro.2019.119707.

[9] R.L. Siegelman, E.J. Kim, J.R. Long, Porous materials for carbon dioxide separations, Nat. Mater. 20 (2021) 1060–1072, https://doi.org/10.1038/s41563-021-01054-8.

[10] O. Cheung, N. Hedin, Zeolites and related sorbents with narrow pores for $CO_2$ separation from flue gas, RSC Adv. 4 (2014) 14480–14494, https://doi.org/10.1039/c3ra48052f.

[11] N. Chanut, A. Ghoufi, M.V. Coulet, S. Bourrelly, B. Kuchta, G. Maurin, P.L. Llewellyn, Tailoring the separation properties of flexible metal-organic frameworks using mechanical pressure, Nat. Commun. 11 (2020) 1–7, https://doi.org/10.1038/s41467-020-15036-y.

[12] J.A. Cecilia, E. Vilarrasa-García, R. Morales-Ospino, M. Bastos-Neto, D.C.S. Azevedo, E. Rodríguez-Castellón, Insights into $CO_2$ adsorption in amino-functionalized SBA-15 synthesized at different aging temperature, Adsorption 26 (2020) 225–240, https://doi.org/10.1007/s10450-019-00118-1.

[13] A.E. Creamer, B. Gao, Carbon-based adsorbents for postcombustion $CO_2$ capture: a critical review, Environ. Sci. Technol. 50 (2016) 7276–7289, https://doi.org/10.1021/acs.est.6b00627.

[14] S.G. Subraveti, S. Roussanaly, R. Anantharaman, L. Riboldi, A. Rajendran, How much can novel solid sorbents reduce the cost of post-combustion $CO_2$ capture? A techno-economic investigation on the cost limits of pressure–vacuum swing adsorption, Appl. Energy 306 (2022), 117955, https://doi.org/10.1016/j.apenergy.2021.117955.

[15] K. Sumida, D.L. Rogow, J.A. Mason, T.M. McDonald, E.D. Bloch, Z.R. Herm, T.H. Bae, J.R. Long, Carbon dioxide capture by metal organic frameworks, Chem. Rev. 112 (2012) 724–781, https://doi.org/10.1021/cr2003272.

[16] C. Song, W. Pan, S.T. Srimat, J. Zheng, Y. Li, Y. Wang, B. Xu, Q. Zhu, Tri-reforming of methane over Ni catalysts for $CO_2$ conversion to syngas with desired $H_2/CO$ ratios using flue gas of power plants without $CO_2$ separation, Stud. Surf. Sci. Catal. 153 (2004) 315–322.

[17] K.J. Chen, D.G. Madden, T. Pham, K.A. Forrest, A. Kumar, Q.Y. Yang, W. Xue, B. Space, J.J. Perry, J.P. Zhang, X.M. Chen, M.J. Zaworotko, Tuning pore size in square-lattice coordination networks for size-selective sieving of $CO_2$, Angew. Chem. Int. Ed. 55 (2016) 10268–10272, https://doi.org/10.1002/anie.201603934.

[18] A.A. Azmi, M.A.A. Aziz, Mesoporous adsorbent for $CO_2$ capture application under mild condition: a review, J. Environ. Chem. Eng. 7 (2019), 103022, https://doi.org/10.1016/j.jece.2019.103022.

[19] A. Modak, S. Jana, Advancement in porous adsorbents for post-combustion $CO_2$ capture, Microporous Mesoporous Mater. 276 (2019) 107–132, https://doi.org/10.1016/j.micromeso.2018.09.018.

[20] W. Jeong, J. Kim, Understanding the mechanisms of $CO_2$ adsorption enhancement in pure silica zeolites under humid conditions, J. Phys. Chem. C 120 (2016) 23500–23510, https://doi.org/10.1021/acs.jpcc.6b06571.

[21] I. Erucar, S. Keskin, Unlocking the effect of $H_2O$ on $CO_2$ separation performance of promising MOFs using atomically detailed simulations, Ind. Eng. Chem. Res. 59 (2020) 3141–3152, https://doi.org/10.1021/acs.iecr.9b05487.

[22] R. Ben-Mansour, N.A.A. Qasem, M.A. Antar, Carbon dioxide adsorption separation from dry and humid $CO_2/N_2$ mixture, Comput. Chem. Eng. 117 (2018) 221–235, https://doi.org/10.1016/j.compchemeng.2018.06.016.

[23] M.A.O. Lourenço, M. Fontana, P. Jagdale, C.F. Pirri, S. Bocchini, Improved $CO_2$ adsorption properties through amine functionalization of multi-walled carbon nanotubes, Chem. Eng. J. 414 (2021), 128763, https://doi.org/10.1016/j.cej.2021.128763.

[24] J. Wu, X. Zhu, F. Yang, T. Ge, R. Wang, Easily-synthesized and low-cost amine-functionalized silica sol-coated structured adsorbents for $CO_2$ capture, Chem. Eng. J. 425 (2021), 131409, https://doi.org/10.1016/j.cej.2021.131409.

[25] Y. Wang, X. Hu, T. Guo, W. Tian, J. Hao, Q. Guo, The competitive adsorption mechanism of $CO_2$, $H_2O$ and $O_2$ on a solid amine adsorbent, Chem. Eng. J. 416 (2021) 129007, https://doi.org/10.1016/j.cej.2021.129007.

[26] F. Su, C. Lu, W. Cnen, H. Bai, J.F. Hwang, Capture of $CO_2$ from flue gas via multiwalled carbon nanotubes, Sci. Total Environ. 407 (2009) 3017–3023, https://doi.org/10.1016/j.scitotenv.2009.01.007.

[27] C. Yu, Q. Ding, J. Hu, Q. Wang, X. Cui, H. Xing, Selective capture of carbon dioxide from humid gases over a wide temperature range using a robust metal–organic framework, Chem. Eng. J. 405 (2021), 126937, https://doi.org/10.1016/j.cej.2020.126937.

[28] A. Masala, J.G. Vitillo, G. Mondino, C.A. Grande, R. Blom, M. Manzoli, M. Marshall, S. Bordiga, $CO_2$ capture in dry and wet conditions in UTSA-16 metal-organic framework, ACS Appl. Mater. Interfaces 9 (2017) 455–463, https://doi.org/10.1021/acsami.6b13216.

[29] J. Rogacka, A. Seremak, A. Luna-Triguero, F. Formalik, I. Matito-Martos, L. Firlej, S. Calero, B. Kuchta, High-throughput screening of metal – organic frameworks for $CO_2$ and $CH_4$ separation in the presence of water, Chem. Eng. J. 403 (2021), https://doi.org/10.1016/j.cej.2020.126392.

[30] P.A. Sáenz Cavazos, M.L. Díaz-Ramírez, E. Hunter-Sellars, S.R. McIntyre, E. Lima, I.A. Ibarra, D.R. Williams, Fluorinated MIL-101 for carbon capture utilisation and storage: uptake and diffusion studies under relevant industrial conditions, RSC Adv. 11 (2021) 13304–13310, https://doi.org/10.1039/d1ra01118a.
[31] D.G. Madden, A.B. Albadarin, D. O'Nolan, P. Cronin, J.J. Perry, S. Solomon, T. Curtin, M. Khraisheh, M.J. Zaworotko, G.M. Walker, Metal-organic material polymer coatings for enhanced gas sorption performance and hydrolytic stability under humid conditions, ACS Appl. Mater. Interfaces 12 (2020) 33759–33764, https://doi.org/10.1021/acsami.0c08078.
[32] B.L. Suh, S. Lee, J. Kim, Size-matching ligand insertion in MOF-74 for enhanced $CO_2$ capture under humid conditions, J. Phys. Chem. C 121 (2017) 24444–24451, https://doi.org/10.1021/acs.jpcc.7b08239.
[33] D. Madden, T. Curtin, Carbon dioxide capture with amino-functionalised zeolite-β: a temperature programmed desorption study under dry and humid conditions, Microporous Mesoporous Mater. 228 (2016) 310–317, https://doi.org/10.1016/j.micromeso.2016.03.041.
[34] D. Kwon, J.C. Kim, H. Lee, W. Lee, C. Jo, Engineering micropore walls of beta zeolites by post-functionalization for $CO_2$ adsorption performance screening under humid conditions, Chem. Eng. J. 427 (2022), 131461, https://doi.org/10.1016/j.cej.2021.131461.
[35] J. Zhou, X. Wang, W. Xing, Carbon-based $CO_2$ Adsorbents, The Royal Society of Chemistry, 2019.
[36] J. Kossmann, R. Rothe, T. Heil, M. Antonietti, N. López-Salas, Ultrahigh water sorption on highly nitrogen doped carbonaceous materials derived from uric acid, J. Colloid Interface Sci. 602 (2021) 880–888, https://doi.org/10.1016/j.jcis.2021.06.012.
[37] L. Liu, S. Johnathan Tan, T. Horikawa, D.D. Do, D. Nicholson, J. Liu, Water adsorption on carbon - a review, Adv. Colloid Interface Sci. 250 (2017) 64–78, https://doi.org/10.1016/j.cis.2017.10.002.
[38] K.V. Kumar, K. Preuss, Z.X. Guo, M.M. Titirici, Understanding the hydrophilicity and water adsorption behavior of nanoporous nitrogen-doped carbons, J. Phys. Chem. C 120 (2016) 18167–18179, https://doi.org/10.1021/acs.jpcc.6b06555.
[39] R. Guillet-Nicolas, F. Bérubé, M. Thommes, M.T. Janicke, F. Kleitz, Selectively tuned pore condensation and hysteresis behavior in mesoporous SBA-15 silica: correlating material synthesis to advanced gas adsorption analysis, J. Phys. Chem. C 121 (2017), https://doi.org/10.1021/acs.jpcc.7b06745.
[40] E. Maruccia, M.A.O. Lourenço, T. Priamushko, M. Bartoli, S. Bocchini, F.C. Pirri, G. Saracco, F. Kleitz, C. Gerbaldi, Nanocast nitrogen-containing ordered mesoporous carbons from glucosamine for selective $CO_2$ capture, Mater. Today Sustain. 17 (2022), 100089, https://doi.org/10.1016/j.mtsust.2021.100089.
[41] L. Lefrancois Perreault, S. Giret, M. Gagnon, J. Florek, D. Larivière, F. Kleitz, Functionalization of mesoporous carbon materials for selective separation of lanthanides under acidic conditions, ACS Appl. Mater. Interfaces 9 (2017) 12003–12012, https://doi.org/10.1021/acsami.6b16650.
[42] T.W. Kim, F. Kleitz, B. Paul, R. Ryoo, MCM-48-like large mesoporous silicas with tailored pore structure: facile synthesis domain in a ternary triblock copolymer-butanol-water system, J. Am. Chem. Soc. 127 (2005) 7601–7610, https://doi.org/10.1021/ja042601m.
[43] D. Zhao, J. Feng, Q. Huo, N. Melosh, G.H. Fredrickson, B.F. Chmelka, G.D. Stucky, Triblock copolymer syntheses of mesoporous silica with periodic 50 to 300 angstrom pores, Science 279 (1998) 548–552, https://doi.org/10.1126/science.279.5350.548 (80-.).
[44] S.H. Joo, R. Ryoo, M. Kruk, M. Jaroniec, Evidence for general nature of pore interconnectivity in 2-dimensional hexagonal mesoporous silicas prepared using block copolymer templates, J. Phys. Chem. B 106 (2002) 4640–4646, https://doi.org/10.1021/jp013583n.
[45] L. Gao, A. Chandra, Y. Nabae, T. Hayakawa, Inducing defects in ordered mesoporous carbons via the block copolymerlated high temperature carbonization of nitrogen-containing polymeric precursors, Polym. J. 50 (2018) 389–396, https://doi.org/10.1038/s41428-018-0023-0.
[46] Q. Li, J. Yang, D. Feng, Z. Wu, Q. Wu, S.S. Park, C.S. Ha, D. Zhao, Facile synthesis of porous carbon nitride spheres with hierarchical three-dimensional mesostructures for $CO_2$ capture, Nano Res. 3 (2010) 632–642, https://doi.org/10.1007/s12274-010-0023-7.
[47] M. Thommes, K. Kaneko, A.V. Neimark, J.P. Olivier, F. Rodriguez-Reinoso, J. Rouquerol, K.S.W. Sing, Physisorption of gases, with special reference to the evaluation of surface area and pore size distribution (IUPAC Technical Report), Pure Appl. Chem. 87 (2015) 1051–1069, https://doi.org/10.1515/pac-2014-1117.
[48] K.A. Cychosz, R. Guillet-Nicolas, J. García-Martínez, M. Thommes, Recent advances in the textural characterization of hierarchically structured nanoporous materials, Chem. Soc. Rev. 46 (2017) 389–414, https://doi.org/10.1039/c6cs00391e.
[49] M. Thommes, K.A. Cychosz, Physical adsorption characterization of nanoporous materials: progress and challenges, Adsorption 20 (2014) 233–250, https://doi.org/10.1007/s10450-014-9606-z.
[50] G.Y. Gor, M. Thommes, K.A. Cychosz, A.V. Neimark, Quenched solid density functional theory method for characterization of mesoporous carbons by nitrogen adsorption, Carbon 50 (2012) 1583–1590, https://doi.org/10.1016/j.carbon.2011.11.037.
[51] A.V. Neimark, Y. Lin, P.I. Ravikovitch, M. Thommes, Quenched solid density functional theory and pore size analysis of micro-mesoporous carbons, Carbon 47 (2009) 1617–1628, https://doi.org/10.1016/J.CARBON.2009.01.050.
[52] J. Landers, G.Y. Gor, A.V. Neimark, Density functional theory methods for characterization of porous materials, Colloids Surfaces A Physicochem. Eng. Asp. 437 (2013) 3–32, https://doi.org/10.1016/J.COLSURFA.2013.01.007.
[53] E. Zhang, M.E. Casco, F. Xu, W.B. Sheng, S. Oswald, L. Giebeler, K. Wegner, L. Borchardt, S. Kaskel, On the origin of mesopore collapse in functionalized porous carbons, Carbon N. Y. 149 (2019) 743–749, https://doi.org/10.1016/j.carbon.2019.04.116.
[54] X. Wu, W. Xing, J. Florek, J. Zhou, G. Wang, S. Zhuo, Q. Xue, Z. Yan, F. Kleitz, On the origin of the high capacitance of carbon derived from seaweed with an apparently low surface area, J. Mater. Chem. A 2 (2014) 18998–19004, https://doi.org/10.1039/C4TA03430A.
[55] M. Gehring, H. Tempel, A. Merlen, R. Schierholz, R.A. Eichel, H. Kungl, Carbonisation temperature dependence of electrochemical activity of nitrogen-doped carbon fibres from electrospinning as air-cathodes for aqueous-alkaline metal-air batteries, RSC Adv. 9 (2019) 27231–27241, https://doi.org/10.1039/c9ra03805a.
[56] H. Seema, K.C. Kemp, N.H. Le, S. Park, V. Chandra, J.W. Lee, K.S. Kim, Highly selective $CO_2$ capture by S-doped microporous carbon materials, Carbon 66 (2014) 320–326, https://doi.org/10.1016/j.carbon.2013.09.006.
[57] D. Li, W.B. Li, J.S. Shi, F.W. Xin, Influence of doping nitrogen, sulfur, and phosphorus on activated carbons for gas adsorption of $H_2$, $CH_4$ and $CO_2$, RSC Adv. 6 (2016) 50138–50143, https://doi.org/10.1039/C6RA06620H.
[58] Y. Xia, Preparation of sulfur-doped microporous carbons for the storage of hydrogen and carbon dioxide, Carbon N. Y. 50 (2012) 5543–5553, https://doi.org/10.1016/j.carbon.2012.07.044.
[59] Y. Sun, J. Zhao, J. Wang, N. Tang, R. Zhao, D. Zhang, T. Guan, K. Li, Sulfur-doped millimeter-sized microporous activated carbon spheres derived from sulfonated poly (styrene–divinylbenzene) for $CO_2$ capture, J. Phys. Chem. C (2017) 10000–10009, https://doi.org/10.1021/acs.jpcc.7b02195.
[60] X. Ma, L. Li, R. Chen, C. Wang, K. Zhou, H. Li, Doping of alkali metals in carbon frameworks for enhancing $CO_2$ capture : a theoretical study, Fuel 236 (2019) 942–948, https://doi.org/10.1016/j.fuel.2018.08.166.
[61] M. Ayiania, M. Smith, A.J.R. Hensley, L. Scudiero, J.S. McEwen, M. Garcia-Perez, Deconvoluting the XPS spectra for nitrogen-doped chars: an analysis from first principles, Carbon N. Y. 162 (2020) 528–544, https://doi.org/10.1016/j.carbon.2020.02.065.
[62] Y. Wang, X. Hu, J. Hao, R. Ma, Q. Guo, H. Gao, H. Bai, Nitrogen and oxygen codoped porous carbon with superior $CO_2$ adsorption performance: a combined experimental and DFT calculation study, Ind. Eng. Chem. Res. 58 (2019) 13390–13400, https://doi.org/10.1021/acs.iecr.9b01454.
[63] K. Stańczyk, R. Dziembaj, Z. Piwowarska, S. Witkowski, Transformation of nitrogen structures in carbonization of model compounds determined by XPS, Carbon 33 (1995) 1383–1392, https://doi.org/10.1016/0008-6223(95)00084-Q.
[64] A. Gonciaruk, M.R. Hall, M.W. Fay, C.D.J. Parmenter, C.H. Vane, A.N. Khlobystov, N. Ripepi, Kerogen nanoscale structure and $CO_2$ adsorption in shale micropores, Sci. Rep. 11 (2021) 1–13, https://doi.org/10.1038/s41598-021-83179-z.
[65] A. Nuhnen, C. Janiak, A practical guide to calculate the isosteric heat/enthalpy of adsorption: via adsorption isotherms in metal-organic frameworks, MOFs, Dalton Trans. 49 (2020) 10295–10307, https://doi.org/10.1039/d0dt01784a.
[66] A. Samanta, A. Zhao, G.K.H. Shimizu, P. Sarkar, R. Gupta, Post-combustion $CO_2$ capture using solid sorbents: a review, Ind. Eng. Chem. Res. 51 (2012) 1438–1463, https://doi.org/10.1021/ie200686q.
[67] Y. Zhao, X. Liu, Y. Han, Microporous carbonaceous adsorbents for $CO_2$ separation via selective adsorption, RSC Adv. 5 (2015) 30310–30330, https://doi.org/10.1039/c5ra00569h.
[68] Z. Zhang, J. Zhou, W. Xing, Q. Xue, Z. Yan, S. Zhuo, S.Z. Qiao, Critical role of small micropores in high $CO_2$ uptake, Phys. Chem. Chem. Phys. 15 (2013) 2523–2529, https://doi.org/10.1039/c2cp44436d.
[69] Á. Sánchez-Sánchez, F. Suárez-García, A. Martínez-Alonso, J.M.D. Tascón, Influence of porous texture and surface chemistry on the $CO_2$ adsorption capacity of porous carbons: acidic and basic site interactions, ACS Appl. Mater. Interfaces 6 (2014) 21237–21247, https://doi.org/10.1021/am506176e.
[70] S.D. Kenarsari, D. Yang, G. Jiang, S. Zhang, J. Wang, A.G. Russell, Q. Wei, M. Fan, Review of recent advances in carbon dioxide separation and capture, RSC Adv. 3 (2013) 22739–22773, https://doi.org/10.1039/c3ra43965h.
[71] B. Petrovic, M. Gorbounov, S. Masoudi Soltani, Influence of surface modification on selective $CO_2$ adsorption: a technical review on mechanisms and methods, Microporous Mesoporous Mater. 312 (2021), 110751, https://doi.org/10.1016/j.micromeso.2020.110751.
[72] P. Pornaroontham, G. Panomsuwan, S. Chae, N. Saito, N. Thouchprasitchai, Y. Phongboonchoo, S. Pongstabodee, Nitriding an oxygen-doped nanocarbonaceous sorbent synthesized via solution plasma process for improving $CO_2$ adsorption capacity, Nanomaterials 9 (2019), https://doi.org/10.3390/nano9121776.
[73] G. Lim, K.B. Lee, H.C. Ham, Effect of N-containing functional groups on $CO_2$ adsorption of carbonaceous materials: a density functional theory approach,

J. Phys. Chem. C 120 (2016) 8087–8095, https://doi.org/10.1021/acs.jpcc.5b12090.

[74] T. Horikawa, N. Sakao, D.D. Do, Effects of temperature on water adsorption on controlled microporous and mesoporous carbonaceous solids, Carbon 56 (2013) 183–192, https://doi.org/10.1016/j.carbon.2013.01.003.

[75] J. Fujiki, K. Yogo, Water adsorption on nitrogen-doped carbons for adsorption heat pump/desiccant cooling: experimental and density functional theory calculation studies, Appl. Surf. Sci. 492 (2019) 776–784, https://doi.org/10.1016/j.apsusc.2019.06.267.

[76] J. Heske, R. Walczak, J.D. Epping, S. Youk, S.K. Sahoo, M. Antonietti, T.D. Kühne, M. Oschatz, When water becomes an integral part of carbon – combining theory and experiment to understand the zeolite-like water adsorption properties of porous $C_2N$ materials, J. Mater. Chem. A. 9 (2021) 22563–22572, https://doi.org/10.1039/d1ta05122a.

[77] C. Urita, K. Urita, T. Araki, K. Horio, M. Yoshida, I. Moriguchi, New insights into the heat of adsorption of water, acetonitrile, and n-hexane in porous carbon with oxygen functional groups, J. Colloid Interface Sci. 552 (2019) 412–417, https://doi.org/10.1016/j.jcis.2019.05.090.

[78] J.M. Kolle, M. Fayaz, A. Sayari, Understanding the effect of water on $CO_2$ Adsorption, Chem. Rev. 121 (2021) 7280–7345, https://doi.org/10.1021/acs.chemrev.0c00762.

[79] $CH_2$ moieties have been ascribed to paraffins, the presence of which can be assumed to derive from the paraffin oil in the vacuum pump of the apparatus used for the gas adsorption tests. (Hence, small quantities of oil at really low vapour pressure might be adsorbed from the sample during the activation and weight stabilization stages preceding gas adsorption; usually the above-mentioned oil can be released by simply heating).

[80] John Wiley & Sons, Inc. SpectraBase, (n.d.). https://spectrabase.com/(accessed March 21, 2022)..

[81] National Institute of Standards and Technology (NIST)—U.S. Department of Commerce, NIST Standard Reference Database Number 69, (n.d.). https://webbook.nist.gov/cgi/cbook.cgi?Scan=cob10480&Type=IR (accessed March 22, 2022).

[82] G. Socrates, Infrared and Raman Characteristic Group Frequencies, John Wiley & Sons, 2001, https://doi.org/10.1016/0160-9327(81)90159-9.

[83] D.L. Bertuzzi, T.B. Becher, N.M.R. Capreti, J. Amorim, I.D. Jurberg, J.D.M. Jr, C. Ornelas, General protocol to obtain D-glucosamine from biomass residues: shrimp shells, cicada sloughs and cockroaches, Glob. Challenges (2018), 1800046, https://doi.org/10.1002/gch2.201800046.

[84] N.A.A. Qasem, R. Ben-Mansour, Adsorption breakthrough and cycling stability of carbon dioxide separation from $CO_2/N_2/H_2O$ mixture under ambient conditions using 13X and Mg-MOF-74, Appl. Energy 230 (2018) 1093–1107, https://doi.org/10.1016/j.apenergy.2018.09.069.

[85] Q. Al-Naddaf, S. Lawson, A.A. Rownaghi, F. Rezaei, Analysis of dynamic $CO_2$ capture over 13X zeolite monoliths in the presence of $SO_x$, $NO_x$ and humidity, AIChE J. 66 (2020), https://doi.org/10.1002/aic.16297.

[86] M. Miyamoto, S. Ono, K. Kusukami, Y. Oumi, S. Uemiya, High water tolerance of a core–shell-structured zeolite for $CO_2$ adsorptive separation under wet conditions, ChemSusChem 11 (2018) 1756–1760, https://doi.org/10.1002/cssc.201800063.